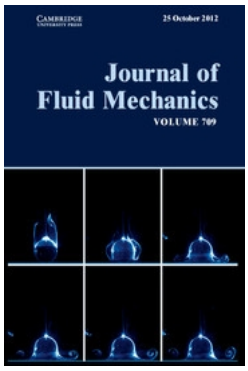

Micro-structure and Lagrangian statistics of the scalar field with a mean gradient in isotropic turbulence

G. BRETHOUWER, J. C. R. HUNT and F. T. M. NIEUWSTADT

Journal of Fluid Mechanics / Volume 474 / January 2003, pp 193 - 225
DOI: 10.1017/S0022112002002549, Published online: 14 January 2003

J. Fluid Mech. (2003), *vol.* 474, *pp.* 193–225.
DOI: 10.1017/S0022112002002549 Printed in the United Kingdom

Micro-structure and Lagrangian statistics of the scalar field with a mean gradient in isotropic turbulence

By G. BRETHOUWER[1]†, J. C. R. HUNT[1,2] AND F. T. M. NIEUWSTADT[1]

[1]J.M. Burgers Centre for Fluid Dynamics, Laboratory for Aero- and Hydrodynamics, Leeghwaterstraat 21, 2628 CA Delft, The Netherlands

[2]Department of Space and Climate Physics, University College London, 17 Gordon Street, London WCIE, UK

(Received 7 September 2001 and in revised form 12 June 2002)

This paper presents an analysis and numerical study of the relations between the small-scale velocity and scalar fields in fully developed isotropic turbulence with random forcing of the large scales and with an imposed constant mean scalar gradient. Simulations have been performed for a range of Reynolds numbers from $Re_\lambda = 22$ to 130 and Schmidt numbers from $Sc = 1/25$ to 144.

The simulations show that for all values of $Sc \geqslant 0.1$ steep scalar gradients are concentrated in intermittently distributed sheet-like structures with a thickness approximately equal to the Batchelor length scale $\eta/Sc^{1/2}$ with η the Kolmogorov length scale. We observe that these sheets or cliffs are preferentially aligned perpendicular to the direction of the mean scalar gradient. Due to this preferential orientation of the cliffs the small-scale scalar field is anisotropic and this is an example of direct coupling between the large- and small-scale fluctuations in a turbulent field. The numerical simulations also show that the steep cliffs are formed by straining motions that compress the scalar field along the imposed mean scalar gradient in a very short time period, proportional to the Kolmogorov time scale. This is valid for the whole range of Sc. The generation of these concentration gradients is amplified by rotation of the scalar gradient in the direction of compressive strain. The combination of high strain rate and the alignment results in a large increase of the scalar gradient and therefore in a large scalar dissipation rate.

These results of our numerical study are discussed in the context of experimental results (Warhaft 2000) and kinematic simulations (Holzer & Siggia 1994). The theoretical arguments developed here follow from earlier work of Batchelor & Townsend (1956), Betchov (1956) and Dresselhaus & Tabor (1991).

1. Introduction

In predicting and controlling many types of industrial and environmental processes it is necessary to calculate the intensity of fluctuations, e.g. in the concentration of scalar species. This involves modelling the key mechanisms of turbulent mixing, i.e. advective dispersion by large-scale motions and small-scale molecular mixing.

† Present address: Department of Mechanics, KTH, SE-100 44 Stockholm, Sweden, geert@mech.kth.se

Further insight into turbulent mixing may also result in a better understanding of the dynamics of the turbulence itself (Shraiman & Siggia 2000).

It is instructive to distinguish between the large-scale advective transport of a scalar, the so-called macro-mixing, and the distortion of the scalar field by the small-scale straining and shearing turbulent motions. As a consequence of a turbulent strain, scalar gradients can become larger and the area of iso-scalar surfaces can grow resulting in an intensive molecular diffusion of the scalar and a strong dissipation of scalar fluctuations. This latter process is called micro-mixing and ultimately it leads to a homogeneous scalar distribution such as for example in a stirred vessel, such as a cup of tea and milk. There have been several approaches to investigate macro- and micro-mixing. Two approaches are particularly relevant to the present work.

The first is the 'Lagrangian' approach in which one considers the motion of fluid particles marked with the scalar. Taylor (1921) was the first to show the connection between the statistics of a single fluid particle and turbulent dispersion. Following the work of Richardson (1926) and Batchelor (1952) who both considered the statistics of pairs of particles, Durbin (1980) and Thomson (1990) developed stochastic Lagrangian models for the scalar fluctuations in a plume and their probability density functions (Sawford 2001). These methods have been extended to incorporate a binary chemical reaction between two species (Komori *et al.* 1991; van Dop 2001) and have been verified experimentally. They have also been applied to estimate quite complex aspects of mixing such as the effect of varying the Reynolds and Schmidt numbers and to estimate how the macro- and micro-mixing processes depend on the Reynolds number (Sawford & Hunt 1986; Borgas & Sawford 1996). These stochastic models, however, depend on unproven concepts about micro-mixing mechanisms. Fung *et al.* (1992) investigated the separation of particle pairs in a turbulent-like flow generated by kinematic simulation and concluded that structures in a turbulent flow field play an important role in the separation of particle pairs, so that statistical models may need some correction. In vortical structures particle pairs stay close together whereas in straining regions pairs can suddenly separate rapidly leading to an intermittent behaviour of particle-pair separation and hence of the mixing process (Fung & Vassilicos 1998; Jullien, Paret & Tabeling 1999).

The second approach to the study of turbulent mixing of scalars is to focus on the small-scale processes and on the evolution of the local velocity and scalar fields. Batchelor (1959), Kraichnan (1974) and Kerstein (2001) and many other researchers (see Frisch 1995 and references therein) carried out a theoretical analysis based on physical assumptions about the statistics of locally homogeneous flow fields. Detailed numerical simulations (Ashurst *et al.* 1987) and experiments (Buch & Dahm 1996, 1998; Warhaft 2000) have led to a better understanding of these theoretical predictions. Kraichnan (1974) has considered the smallest length scales of the scalar field assuming a Schmidt number $Sc > 1$ and that the small scales of the scalar field are subject to a uniform random strain field with a very short correlation time. Kraichnan's model predicts a k^{-1} regime in the scalar spectrum and a scaling with the Batchelor length scale $\eta_B = \eta/Sc^{1/2}$. According to recent direct numerical simulations (DNS) (Bogucki, Domaradzki & Yeung 1997; Brethouwer & Nieuwstadt 1999; Brethouwer 2000) the Kraichnan model leads to the best quantitative prediction of the scalar spectra at high wavenumbers for $Sc > 1$. When $Sc < 1$ and molecular diffusion becomes larger, the scalar spectra at high wavenumbers are still reasonably described by the Kraichnan model including the scaling by the Batchelor length scale despite the fact that the theory is apparently outside its range of validity (Brethouwer & Nieuwstadt 1999; Brethouwer 2000; Orlandi & Antonia 2002).

In some recent numerical and experimental studies the topology of the scalar field has been investigated for both low and high Schmidt numbers. Visualizations of the scalar field show that for $Sc \gg 1$ the dominant structure is a thin sheet (Buch & Dahm 1996). Such a sheet-like structure can be expected on the basis of the observation that the intermediate eigenvalue of the strain tensor is usually positive in a turbulent flow (Betchov 1956; Ashurst *et al.* 1987) so that there are usually two extensional and one compressive principal strain axes (Buch & Dahm 1996; Brethouwer 2000). The sheets are in fact steep jumps or sharp 'cliffs' in the scalar field and they are observed over a wide range of Schmidt numbers, for $Sc \gg 1$ (Buch & Dahm 1996), $Sc \simeq 1$ (Buch & Dahm 1998; Ruetsch & Maxey 1992; Nomura & Elghobashi 1992) and $Sc = 1/8$ (Vedula, Yeung & Fox 2001). A sheet-like structure seems therefore to be a universal characteristic of the micro-structure of a scalar field independent of the Schmidt number. The sheet-like structures result in a very intermittent scalar gradient field (Métais & Lesieur 1992; Sreenivasan & Antonia 1997). Buch & Dahm (1996, 1998) show that a considerable part of the total micro-mixing takes place in these sheets.

The classical view due to Taylor–Kolmogorov of small-scale velocity and scalar fields in fully developed turbulence is that the small scales are not directly affected by large-scale conditions and therefore must be locally isotropic (Monin & Yaglom 1975). However, this view does not agree with measurements of higher moments in turbulent flows with anisotropic or intermittent large-scale motions or anisotropic forcing (Frisch 1995; Hunt, Kaimal & Gaynor 1988; Sreenivasan & Antonia 1997). In the case of an imposed mean scalar gradient, experimental measurements and numerical simulations show that gradients aligned with the imposed mean gradient are on average larger than those perpendicular to the mean gradient (Mydlarski & Warhaft 1998; Pumir 1994; Overholt & Pope 1996; Warhaft 2000). The data do not indicate that the small scales tend to become isotropic as the Reynolds number increases although there is some discussion about how to interpret the results (Kurien, Aivalis & Sreenivasan 2001).

Holzer & Siggia (1994) simulated the mixing of a scalar with an imposed mean gradient in an isotropic turbulent-like flow field and observed that the scalar field has a ramp–cliff structure, i.e. regions of well-mixed fluid with a nearly constant scalar concentration bounded by steep cliffs. These ramp–cliff structures are positioned approximately perpendicular to the mean gradient. The visualizations of Holzer & Siggia suggest that the cliffs are generated by large-scale straining motions with the direction of compression approximately aligned with the mean scalar gradient.

In this paper we study turbulent mixing of a passive scalar with an imposed mean gradient by isotropic turbulence with the help of DNS and over a wide range of Schmidt numbers. The goal of our investigation is to find answers to the following points:

(i) What is the micro-structure of the scalar field and how does it depend on the Schmidt number? Furthermore, what is the relation between the micro-structure and the imposed mean scalar gradient?

(ii) How is the scalar gradient field and the formation of cliffs related to the eddy structure? What is the influence of strain at low and high Schmidt numbers and what is the role of vorticity? With respect to the role of vorticity, dynamical studies (Ruetsch & Maxey 1991, 1992) show that scalar sheets may roll up into tube-like structures but quantitative results presented by Zhou & Antonia (2000) and by Pumir (1994) suggest that the vorticity has only a minor influence on scalar gradients.

(iii) Is the scalar mixing process also intermittent in a Lagrangian frame and how

does the scalar gradient field respond to the dynamics of the turbulence? For instance, the Lagrangian study of Fung *et al.* (1992) shows that the separation of fluid particle pairs is a very intermittent process and is related to the eddy structure.

The outline of this paper is as follows: We first present and discuss in § 2 the governing equations for the scalar gradient. Then we discuss briefly the invariants of the velocity gradient tensor and their relation to the local flow topology. These invariants are used later in the paper to study the relation between turbulent structures and the micro-structure of the scalar field. Then we present our numerical simulations. We study the micro-structure of the scalar field in the presence of a mean gradient and some characteristics of the scalar gradient cliffs, in relation to the turbulent structures using the concepts presented in § 2. We end this paper with the conclusions.

2. Analyses of scalar gradients

To provide the background for the analyses to be presented later we discuss here some relations and properties of a scalar gradient in a turbulent flow. Let us assume that the instantaneous passive scalar concentration Θ is given by

$$\Theta = \theta + \boldsymbol{G} \cdot \boldsymbol{x}, \tag{2.1}$$

where $\boldsymbol{G}$ is the mean scalar gradient and θ is the scalar fluctuation which satisfies $\langle \theta \rangle = 0$. The angular brackets can be interpreted as an ensemble average which in the case of the homogeneous turbulence considered here can be computed as the spatial average over the whole turbulence field. The equation for θ in an incompressible isothermal flow field then reads

$$\frac{\mathrm{d}\theta}{\mathrm{d}t} = \frac{\partial \theta}{\partial t} + \boldsymbol{u} \cdot \nabla \theta = -\boldsymbol{G} \cdot \boldsymbol{u} + \kappa \nabla^2 \theta, \tag{2.2}$$

where κ is the diffusivity of the scalar. The term $\boldsymbol{G} \cdot \boldsymbol{u}$ can be interpreted as a source of scalar fluctuations because in a steady-state situation it balances the destruction of scalar fluctuations by molecular dissipation as expressed by

$$0 = -\langle \theta \boldsymbol{G} \cdot \boldsymbol{u} \rangle - \chi, \tag{2.3}$$

where $\chi = \kappa \langle (\nabla \theta)^2 \rangle$.

The relation between the scalar gradient $\nabla \theta$ and the straining of the velocity field, derived by Corrsin (1953) and Batchelor & Townsend (1956), is given by

$$\frac{\mathrm{d}\nabla \theta}{\mathrm{d}t} = -\nabla \theta \cdot \boldsymbol{S} - \boldsymbol{G} \cdot \boldsymbol{S} - \tfrac{1}{2} \nabla \theta \times \boldsymbol{\omega} - \tfrac{1}{2} \boldsymbol{G} \times \boldsymbol{\omega} + \kappa \nabla^2 \nabla \theta, \tag{2.4}$$

which shows that the concentration gradient depends on the rate-of-strain tensor, $S_{ij} = \frac{1}{2}(\partial u_i / \partial x_j + \partial u_j / \partial x_i)$ and the vorticity vector $\boldsymbol{\omega}$.

With the help of relation (2.4) we can now analyse in more detail the amplification and alignment of scalar gradients by using the results of Dresselhaus & Tabor (1991) for the stretching of line elements and their alignment with the principal axes of strain in a general flow field. First, it is convenient to give some definitions. Let us assume that the coordinate system coincides with the principal axes of strain. In that case the only non-zero terms in the strain-rate tensor are the terms on the diagonal, which are denoted as principal strain rates, $\mathscr{S}_\alpha, \mathscr{S}_\beta, \mathscr{S}_\gamma$ with $\mathscr{S}_\gamma \leqslant \mathscr{S}_\beta \leqslant \mathscr{S}_\alpha$. For incompressible flows, as considered here, it follows that $\mathscr{S}_\alpha + \mathscr{S}_\beta + \mathscr{S}_\gamma = 0$. Consequently, $\mathscr{S}_\gamma$ must be negative and $\mathscr{S}_\alpha$ positive while $\mathscr{S}_\beta$ can have either sign. The corresponding unit vectors along the principal axes of strain are denoted by $\boldsymbol{e}_\gamma, \boldsymbol{e}_\beta, \boldsymbol{e}_\alpha$. Furthermore, we

introduce the unit vector $\boldsymbol{n} = \nabla\theta/|\nabla\theta|$ in the direction of the scalar gradient and the alignment vector $\boldsymbol{\lambda}$ with components $\lambda_i = \boldsymbol{n} \cdot \boldsymbol{e}_i$ so that λ_i is the cosine of the angle between $\nabla\theta$ and $\boldsymbol{e}_i$.

Using these definitions and relation (2.4) we can derive the equation for the norm of the scalar gradient $g = (\nabla\theta \cdot \nabla\theta)^{1/2}$:

$$\frac{1}{g}\frac{\mathrm{d}g}{\mathrm{d}t} = -\mathscr{S}_i\lambda_i^2 - \frac{1}{g^2}\boldsymbol{G}\cdot\boldsymbol{S}\cdot\nabla\theta - \frac{1}{2g^2}\nabla\theta\cdot(\boldsymbol{G}\times\boldsymbol{\omega}) + \frac{1}{2g^2}\left(\kappa\nabla^2 g^2 - \epsilon_{\nabla\theta}\right), \tag{2.5}$$

where $\mathscr{S}_i\lambda_i^2 = \mathscr{S}_\alpha\lambda_\alpha^2 + \mathscr{S}_\beta\lambda_\beta^2 + \mathscr{S}_\gamma\lambda_\gamma^2 = \nabla\theta\cdot\boldsymbol{S}\cdot\nabla\theta/g^2$ and $\epsilon_{\nabla\theta} = 2\kappa\nabla(\nabla\theta):\nabla(\nabla\theta)$ is the molecular destruction of scalar gradients. The first three terms on the right-hand side of equation (2.5) can be regarded as production or amplification terms due to strain and vorticity. We note that the first and second production terms depend on the orientation of the scalar gradient with respect to the principal axes of strain. Below we will find that $\nabla\theta$ preferentially aligns with $\boldsymbol{e}_\gamma$ (Ashurst *et al.* 1987). In that case it follows that the first term is of the order of $\mathscr{S}_\gamma$ and the second term is at most $-\mathscr{S}_\gamma|\boldsymbol{G}|/g$. If we assume further that the vorticity is of the same order of magnitude as the strain rate, the third term is probably of the same order as the second term. When Re and Sc are high enough, the ratio $|\boldsymbol{G}|/g$ is small and therefore the second and the third terms on the right-hand side of relation (2.5) can probably be neglected with respect to the first term. This observation is supported by the simulations of Vedula *et al.* (2001).

The equation for the square of the norm of the scalar gradient in one particular direction $g_\ell^2 = (\partial\theta/\partial x_\ell)^2$ (no summation over the index ℓ) is given by (Gonzalez 2000)

$$\frac{\mathrm{d}g_\ell^2}{\mathrm{d}t} = -2\frac{\partial\theta}{\partial x_\ell}S_{\ell i}\frac{\partial\theta}{\partial x_i} - \varepsilon_{\ell ij}\frac{\partial\theta}{\partial x_\ell}\frac{\partial\theta}{\partial x_i}\omega_j - 2\frac{\partial\theta}{\partial x_\ell}\frac{\partial u_i}{\partial x_\ell}G_i - 4\kappa\left(\frac{\partial^2\theta}{\partial x_i\partial x_\ell}\right)^2, \tag{2.6}$$

where $\varepsilon_{\ell ij}$ is the permutation tensor. The first and third terms on the right-hand side of (2.6) are the production terms of g_ℓ^2 and are called the amplification and the mean gradient term respectively in this paper. The second term, called the rotation term, represents redistribution between the different components of g_ℓ^2 because it drops out when the equations for g_ℓ^2 for all three directions are added together leading to (2.5). The total scalar dissipation rate χ is simply the sum of $\kappa\, g_\ell^2$ in all three directions.

For the alignment vector $\boldsymbol{\lambda}$ we can derive a separate equation. First we consider the evolution equations for the vectors $\boldsymbol{n}$ and $\boldsymbol{e}_i$. The equation for $\boldsymbol{n}$ reads

$$\frac{\mathrm{d}\boldsymbol{n}}{\mathrm{d}t} = \frac{\mathrm{d}\nabla\theta/g}{\mathrm{d}t} = \frac{1}{g}\frac{\mathrm{d}\nabla\theta}{\mathrm{d}t} - \frac{\nabla\theta}{g^2}\frac{\mathrm{d}g}{\mathrm{d}t} = -\boldsymbol{n}\cdot\boldsymbol{S}\cdot(\boldsymbol{I}-\boldsymbol{nn}) - \tfrac{1}{2}\boldsymbol{n}\times\boldsymbol{\omega} + \kappa\frac{\nabla^2(\nabla\theta)}{g}\cdot(\boldsymbol{I}-\boldsymbol{nn}), \tag{2.7}$$

where $\boldsymbol{I}$ is the unit tensor. In the derivation of this equation we have neglected all terms of order $|\boldsymbol{G}|/g$.

The equation for $\boldsymbol{e}_i$ is given by

$$\frac{\mathrm{d}\boldsymbol{e}_i}{\mathrm{d}t} = \boldsymbol{\varphi}\times\boldsymbol{e}_i. \tag{2.8}$$

The $\boldsymbol{\varphi}$ is the strain rotation vector given by

$$\varphi_k = \epsilon_{ijk}(-\tfrac{1}{4}\omega_i\omega_j - \partial^2 p/\partial x_i\partial x_j + \nu(\nabla^2\boldsymbol{S})_{ij})/(\mathscr{S}_i - \mathscr{S}_j), \tag{2.9}$$

where p is the pressure (Dresselhaus & Tabor 1991).

With help of (2.7) and (2.8) and by neglecting in the derivation all terms that are of order $|\boldsymbol{G}|/g$, we can derive for the evolution of $\boldsymbol{\lambda}$:

$$\frac{\mathrm{d}\boldsymbol{\lambda}}{\mathrm{d}t} = \boldsymbol{\sigma}\cdot\boldsymbol{\lambda} + \boldsymbol{\mathscr{R}}\times\boldsymbol{\lambda} + \kappa\frac{\nabla^2(\nabla\theta)}{g}\cdot(\boldsymbol{I}-\boldsymbol{nn})\cdot\mathbf{e}. \tag{2.10}$$

Here $\mathbf{e} = (\boldsymbol{e}_\alpha, \boldsymbol{e}_\beta, \boldsymbol{e}_\gamma)$ and $\boldsymbol{\sigma}$ is given by

$$\boldsymbol{\sigma} = \mathscr{S}_i\lambda_i^2\boldsymbol{I} - \begin{pmatrix} \mathscr{S}_\alpha & 0 & 0 \\ 0 & \mathscr{S}_\beta & 0 \\ 0 & 0 & \mathscr{S}_\gamma \end{pmatrix}, \tag{2.11}$$

and the vector $\boldsymbol{\mathscr{R}}$ by

$$\boldsymbol{\mathscr{R}} = \tfrac{1}{2}\boldsymbol{\omega} - \boldsymbol{\varphi}. \tag{2.12}$$

Based on the equations derived above we now consider how the development of the scalar gradient depends on the strain rate and the vorticity. Let us start with the influence of the strain rate. The first term on the right-hand side of equation (2.5) shows that the compressive strain $\mathscr{S}_\gamma$ amplifies scalar gradients. This amplification is maximal when the scalar gradient is aligned with $\boldsymbol{e}_\gamma$, i.e. $\lambda_\gamma = 1$. In this case the scalar gradient grows exponentially fast if molecular diffusion can be neglected. If the scalar gradient does not align with $\boldsymbol{e}_\gamma$ the production term is much smaller and can even become negative, for example when $\nabla\theta$ is aligned with $\boldsymbol{e}_\alpha$.

As shown by (2.10) the alignment depends on the strain itself. It follows for instance from (2.11) that $\sigma_\alpha \leqslant 0$, $\sigma_\gamma \geqslant 0$ and $\sigma_\gamma \geqslant \sigma_\beta \geqslant \sigma_\alpha$ for an incompressible flow, so that the strain increases λ_γ and decreases λ_α. Therefore, in the case of a pure straining motion the scalar gradient will approach full alignment with $\boldsymbol{e}_\gamma$ and this implies maximal amplification of the scalar gradient.

Let us now consider the effect of vorticity on the scalar gradient. Equation (2.5) shows that the vorticity in combination with the mean gradient may contribute directly to the amplification of scalar gradients. This will be negligible because $|\boldsymbol{G}| \ll g$. The vorticity, however, also has an indirect influence on the orientation of the scalar gradient through the second term on the right-hand side of (2.10), which represents the combined effect of vorticity and rotation of the principal axes of strain. When $\boldsymbol{\mathscr{R}}$ is non-zero the second term rotates $\boldsymbol{\lambda}$ about an axis with direction $\boldsymbol{\mathscr{R}}/|\boldsymbol{\mathscr{R}}|$ and this leads to misalignment between $\nabla\theta$ and $\boldsymbol{e}_\gamma$. Whereas strain tends to align the scalar gradient with $\boldsymbol{e}_\gamma$, large values of vorticity or of the rotation of the principal axes can diminish this alignment. For instance, in the case of a simple shear flow $\boldsymbol{\mathscr{R}}$ is non-zero and therefore the scalar gradient does not fully align with $\boldsymbol{e}_\gamma$ asymptotically. In this case the scalar gradient grows only algebraically whereas in pure strain flow where the vorticity is zero, the scalar gradient grows exponentially. A similar effect has been described by Girimaji & Pope (1990) who found that the mean stretching rate of line elements in a turbulent flow is much lower than what would follow from a prediction based on an assumption of persistent straining. As an explanation they mention a poor alignment between the line element and the direction of the largest stretching and this misalignment was attributed to vorticity and rotation of the principal strain axes.

Vortex stretching and scalar-gradient amplification by strain are closely related. In an inviscid, incompressible flow and for a non-diffusive scalar the following relation between vorticity and the scalar gradient can be derived (Corrsin 1953; Batchelor &

Townsend 1956; Ohkitani 1998):

$$\frac{\mathrm{d}(\nabla\Theta\cdot\boldsymbol{\omega})}{\mathrm{d}t}=0, \tag{2.13}$$

from which for the fluctuating scalar gradient follows:

$$\frac{\mathrm{d}(\nabla\theta\cdot\boldsymbol{\omega})}{\mathrm{d}t}=-\boldsymbol{G}\cdot\boldsymbol{S}\cdot\boldsymbol{\omega}. \tag{2.14}$$

Let us now estimate how the variation of $\nabla\theta\cdot\boldsymbol{\omega}$ compares to the variation of its norm, $g\,\omega$. The equation for $g\,\omega$ is given by

$$\frac{\mathrm{d}g\,\omega}{\mathrm{d}t}=-\frac{\omega}{g}\nabla\theta\cdot\boldsymbol{S}\cdot\nabla\theta+\frac{g}{\omega}\boldsymbol{\omega}\cdot\boldsymbol{S}\cdot\boldsymbol{\omega}, \tag{2.15}$$

where again terms of order $|\boldsymbol{G}|/g$ have been neglected. Let us now consider the first term on the right-hand side of (2.15). In the case of alignment between $\nabla\theta$ and $\boldsymbol{e}_\gamma$ this term equals $-\omega\,g\,\mathscr{S}_\gamma$ which is of order $g/|\boldsymbol{G}|$ times the right-hand side of equation (2.14). The variation of $\nabla\theta\cdot\boldsymbol{\omega}$ is thus small compared to the variation of its norm $g\,\omega$, especially when Re is large.

To obtain more insight let us consider the behaviour of $\nabla\theta\cdot\boldsymbol{\omega}$ in a special case. Consider a three-dimensional straining flow, with $u=-\sigma x$, $v=\sigma y/2$, $w=\sigma z/2$ and $\sigma>0$. The vorticity ω_x is reduced ($\propto\sigma$) while $\nabla\theta_x$ is increased by the strain ($\propto\sigma$). On the other hand ω_y or ω_z are increased by less ($\propto\sigma/2$) while $\nabla\theta_y$ and $\nabla\theta_z$ are decreased. We thus find that those components of the scalar gradient and the vorticity vector that are perpendicular to each other are increased and, as a consequence, $\nabla\theta$ and $\boldsymbol{\omega}$ evolve to an orientation normal to each other. Equation (2.14) leads us then to the following suggestion. If a scalar gradient sheet is generated by a strong compressive straining deformation, the accompanying extensional strains stretch the component of the vorticity components in the plane of the sheet at the same time. This results in the formation of a vortex sheet coinciding with the scalar gradient sheet.

Analytical and numerical studies (Vincent & Meneguzzi 1994; Passot *et al.* 1995) show that when strained vorticity forms sheets, these sheets roll up into vortex tubes either due to Kelvin–Helmholtz instabilities (Passot *et al.* 1995) or due to self-induction caused by the finite width of the sheets (Kevlahan & Hunt 1997). These vortex tubes can wrap the scalar gradient sheets around them (Ruetsch & Maxey 1992). The simulations of Ruetsch & Maxey (1992) indicate that this rolling up process is more efficiently at large Schmidt numbers, for which the thickness of the sheets, $\sim\eta_B$, is smaller than the size of the vortex tubes which are estimated to be proportional to the Kolmogorov length scale. When $Sc\simeq 1$ or $Sc<1$ no rolling up of scalar sheets is expected.

3. Invariants of the velocity gradient tensor and flow topology

The streamline pattern in a small area around a point, as seen by an observer moving with the flow, can be described in terms of the invariants of the velocity gradient tensor $A_{ij}=\partial u_i/\partial x_j$ (Blackburn, Mansour & Cantwell 1996; Chong *et al.* 1998; Ooi *et al.* 1999). The invariants are $Q_A=-\frac{1}{2}A_{ij}A_{ji}$ and $R_A=-\frac{1}{3}A_{ij}A_{jk}A_{ki}$ where Q_A can be expressed alternatively as $Q_A=\frac{1}{4}\omega^2-\frac{1}{2}S_{ij}S_{ij}$. These invariants have been explained in terms of vortex dynamics by Tsinober (2000). Figure 1 presents an illustration of the local flow topology in terms of these invariants. The line $R_A=0$ and

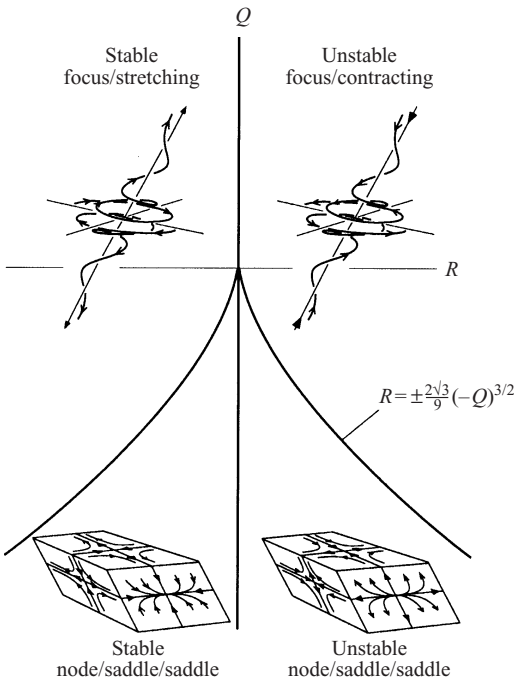

FIGURE 1. Illustrations and terminology of the local flow pattern in terms of the invariants Q_A and R_A for an observer moving with the flow (from Soria *et al.* 1994).

the tent-like curve defined by $D = 0$ with $D = (27/4)R_A^2 + Q_A^3$ divides the (R_A, Q_A)-plane into four regions. Each region corresponds to a different flow topology as illustrated in the figure. The terminology for the flow patterns that we have adopted was proposed by Chong *et al.* (1998).

4. The direct numerical simulation

To study the process of passive scalar mixing we have performed direct numerical simulations (DNS) of three-dimensional isotropic and homogeneous turbulence in a periodic box with equal sides of length 2π. In this box the incompressible Navier–Stokes equations are solved by means of a pseudo-spectral method. For the time integration of the equations an explicit second-order Runge–Kutta scheme is applied. For further details of the numerical code we refer to Debussche, Dubois & Temam (1995).

A statistically stationary turbulent field is simulated by applying a forcing in the form of adding kinetic energy to the largest turbulence scales. This forcing term is only non-zero for $|\boldsymbol{k}| \leqslant k_F$. We have used two different forcing methods. The first method is usually referred to as frozen amplitude forcing and has been applied by Squires & Eaton (1991). The second method is based on a stochastic process and has been proposed by Yeung & Pope (1989).

Simultaneously with the Navier–Stokes equations the advection–diffusion equation (2.2) for a passive and conserved scalar is solved. As a result of the linear mean scalar gradient $\boldsymbol{G}$ which lies in the x-direction, the statistics of the scalar are stationary.

For a DNS the number of modes N per coordinate direction for the velocity should be chosen large enough so that $k_{max}\eta > 1$ where η is the Kolmogorov length

Run	*A*	*B*	*C*	*D*	*E*	*F*	*G*
Re_λ	22	46	90	95	130	85	59
N	64	64	128	128	192	192	64
Forcing	FA	FA	FA	FA	FA	UO	UO
k_F	$2\sqrt{2}$	$2\sqrt{2}$	$2\sqrt{2}$	$2\sqrt{2}$	$2\sqrt{2}$	2.5	$\sqrt{2}$
u'	0.273	0.303	0.315	0.314	0.323	2.007	1.245
ϵ	0.0130	0.0139	0.0146	0.0142	0.0148	3.940	0.688
ℓ	1.682	1.356	1.198	1.194	1.188	1.135	1.584
η	0.1139	0.0480	0.0191	0.0175	0.0117	0.0197	0.0471
$k_{max}\eta$	3.64	1.54	1.22	1.12	1.12	1.65	1.40

TABLE 1. Numerical parameters for the turbulence computations and some Eulerian statistics of the flow. $Re_\lambda = u'\lambda/\nu$: Reynolds number based on the Taylor micro-scale λ and the r.m.s. of the velocity fluctuations u'; N: number of modes per coordinate direction for the turbulence computation; forcing: FA denotes forcing of the velocity field by the frozen amplitude method and UO denotes a forcing by the Uhlenbeck–Ornstein method; k_F: largest forced wavenumber; ϵ: energy dissipation rate; ℓ: integral length scale; η: Kolmogorov length scale; k_{max}: the largest resolved wavenumber.

scale and k_{max} is the largest resolved wavenumber (Eswaran & Pope 1988). All our simulations satisfy this criterion which means that the velocity field is well resolved. Although there is a clear separation of scales between the large-scale almost inviscid motions and the smallest dissipative eddies, the value of Re is not large enough for the existence of a clear inertial subrange (Brethouwer 2000). In flows where $Sc > 1$ the micro-scales of the scalar field are smaller than the Kolmogorov scale. The number of modes N is then not sufficient to obtain a well-resolved scalar field. Therefore, for $Sc > 1$ we have used more modes N_θ for the scalar than for the velocity, i.e. $N_\theta > N$. The value of N_θ is selected based on the criterion that the Batchelor scale $\eta_B = \eta/Sc^{1/2}$ is resolved or $k_{max}\eta_B > 1$. However, we can only solve the advection–diffusion equation in spectral space when we know the Fourier-coefficients of the velocity for all N_θ modes. To achieve this we have taken the unknown Fourier coefficients to be zero in the velocity expansion for wavenumbers above $1-\frac{1}{2}N$ and $\frac{1}{2}N$. This implies a smooth interpolation of the velocity field on the scalar grid at scales smaller than η.

The turbulent simulations that we have carried out are labelled by the letters *A*–*G* and are listed in table 1. In runs *A*, *B*, *C*, *D*, *E* the velocity field is dealiased using the 2/3-rule whereas the scalar field is not dealiased. In runs *F*, *G* the aliasing errors of both the velocity and scalar are reduced by using the phase shifting technique in combination with truncation (Canuto *et al.* 1988).

After the start-up of the simulations the variances of the velocity and scalar fluctuations change from their initial state to a statistical steady state. From this point on, complete three-dimensional data fields of the velocity and the scalar are stored at constant time intervals for post-processing.

The Eulerian statistics that we show in the next sections are volume- and time-averaged over about ten eddy-turnover time scales. In addition to Eulerian statistics of the scalar mixing process, Lagrangian statistics have been computed by calculating the paths of 27 000 fluid particles in the computational domain. These paths are obtained from

$$\frac{\mathrm{d}\boldsymbol{x}^+}{\mathrm{d}t} = \boldsymbol{u}(\boldsymbol{x}^+, t), \tag{4.1}$$

where $\boldsymbol{x}^+$ is the position of the fluid particle at time t. For the time integration of the particle equation we have used a second-order Runge–Kutta scheme. An

Run	Sc	N_θ	Re_λ	$k_{max}\eta_B$	S_χ	K_χ	$\frac{\langle(\nabla_\parallel\theta)^2\rangle}{\langle(\nabla_\perp\theta)^2\rangle}$	$S_{\nabla_\parallel\theta}$	$K_{\nabla_\parallel\theta}$	$K_{\nabla_\perp\theta}$	$\frac{\langle(\nabla_\parallel\theta)^2\rangle^{1/2}}{\lvert\boldsymbol{G}\rvert}$
A	144	256	22	1.22							
B_1	1	96	46	2.30	6.7	75	1.03	1.9	12.9	10.7	5.2
B_2	7	192	46	1.76	7.7	108	1.05	1.4	14.8	12.6	12.8
B_3	25	324	46	1.56	7.6	104	1.01	0.9	14.1	12.9	24.5
C	3	288	90	1.59	8.0	116	1.04	1.3	16.1	13.6	16.2
D_1	0.7	128	95	1.34	7.5	97	1.09	1.8	15.3	12.0	8.0
D_2	0.1	128	95	3.54	7.2	98	1.10	2.0	13.0	9.3	2.9
E_1	0.5	192	130	1.58	8.4	123	1.05	1.8	16.9	14.5	9.1
E_2	0.04	192	130	5.61	6.3	69	1.02	1.7	10.5	8.6	2.4
F	0.7	192	85	1.97	7.9	116	1.11	1.7	14.5	12.0	6.8
G	0.7	64	59	1.68	6.0	62	1.07	1.6	10.6	8.6	4.5

TABLE 2. Numerical parameters for the scalar computations. Sc: Schmidt number; N_θ: number of modes per coordinate direction for the scalar computation; $Re_\lambda = u'\lambda/\nu$: as in table 1; k_{max}: as in table 1; η_B the Batchelor lengths scale; S_χ: skewness of the scalar dissipation χ; K_χ: kurtosis of the scalar dissipation χ; $\langle(\nabla_\parallel\theta)^2\rangle/\langle(\nabla_\perp\theta)^2\rangle$: the ratio of the variance of the scalar gradient parallel and perpendicular to the mean gradient; $S_{\nabla_\parallel\theta}$: skewness of the scalar gradient parallel to the mean gradient; $K_{\nabla_\parallel\theta}$: kurtosis of the scalar gradient parallel to the mean gradient; $K_{\nabla_\perp\theta}$: kurtosis of the scalar gradient perpendicular to the mean gradient; $\langle(\nabla_\parallel\theta)^2\rangle^{1/2}/|\boldsymbol{G}|$ the r.m.s. of scalar gradient parallel to the mean gradient normalized with the imposed mean scalar gradient $\boldsymbol{G}$.

interpolation routine is needed to obtain the velocity $\boldsymbol{u}(\boldsymbol{x}^+, t)$ at the position $\boldsymbol{x}^+$ of the fluid particles. We have used the accurate and well-tested partial Hermite interpolation scheme developed by Balachandar & Maxey (1989) for this purpose. The same interpolation scheme has been used to determine the scalar and velocity gradients at the positions of the fluid particles. The Lagrangian statistics have been collected and stored at small constant time intervals for post-processing.

Some parameters of the simulations and some Eulerian statistics of the flow field are also summarized in table 1. The velocity spectra obtained from the DNS results agree very well with spectra obtained from other DNS (Brethouwer 2000). In table 2 we summarize the basic parameters of the simulations of scalar mixing that we have carried out. The notation of the runs A, B, C, D, E, F, G corresponds to the runs listed in table 1. The subscripts are used to distinguish between runs with the same flow parameters but different Schmidt numbers.

5. Analyses of the numerical results

In this section we present the results of our DNS of passive scalar mixing in the presence of a mean gradient. In § 5.1 the micro-structure of the scalar field and the influence of the mean scalar gradient on the micro-structure is investigated for a wide range of Schmidt numbers. In § 5.2 the relation between the turbulent velocity field and the micro-structure of the scalar field is studied using the relations and analyses presented in section § 2. Finally in § 5.3 we present the Lagrangian statistics which allow us to study the dynamics of turbulent passive scalar mixing.

5.1. *The micro-structure of the scalar field*

Figure 2(*a–d*) shows the instantaneous scalar field on a two-dimensional plane through the computational domain. In figure 2(*a–c*) η_B is approximately equal, between 0.0095 an 0.011 with η largest in figure 2(*a*) and smallest in figure 2(*c*). In figure 2(*d*) η_B

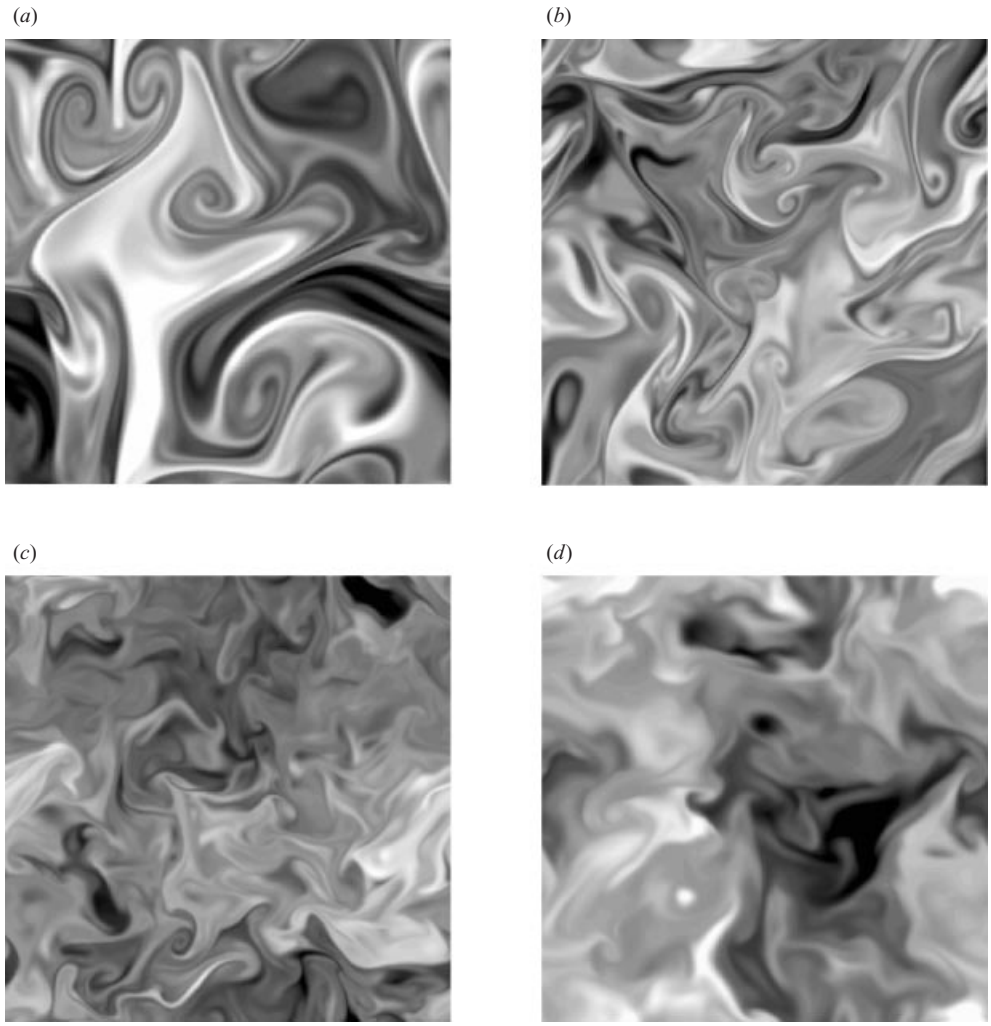

FIGURE 2. The scalar distribution on a two-dimensional plane for (*a*) run *A* with $Sc = 144$ and $Re_\lambda = 22$, (*b*) run B_3 with $Sc = 25$ and $Re_\lambda = 46$, (*c*) run *C* with $Sc = 3$ and $Re_\lambda = 90$ and (*d*) run *F* with $Sc = 0.7$ $Re_\lambda = 85$.

is approximately 2.3 times as large as in the other figures. In figure 2(*a*, *b*) $Sc \gg 1$ and we observe at these high Schmidt numbers thin, elongated structures. Most likely these are cross-sections of sheet-like structures in the scalar field. The existence of sheet-like structures is confirmed in figure 3 where we present a three-dimensional view of the scalar field for $Sc = 25$. Such structures were also observed at $Sc = 2 \times 10^3$ by Buch & Dahm (1996). Figures 2 and 3 show that some of these sheet-like structures are very close and almost parallel to each other. In addition they are more or less flat but at some places they are twisted and folded or even rolled up. The rolling up seems to occur at the end of the scalar sheets. When the Schmidt number decreases we see in figure 2 that it becomes more difficult to distinguish sheet-like structures. We also see that the ratio of their length to their thickness seems to decrease. At $Sc = 3$ some of these sheet-like structures can still be observed, but at $Sc = 0.7$ the existence of scalar sheets is hardly noticeable anymore. At $Sc = 0.7$, however,

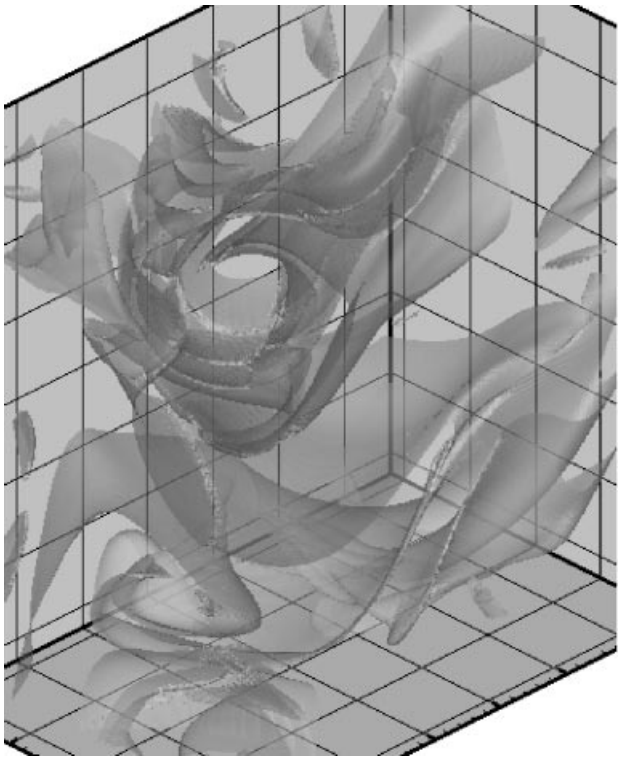

FIGURE 3. A three-dimensional plot of the iso-scalar surface obtained from run B_3 with $Sc = 25$ and $Re_\lambda = 46$.

we observe lumps of almost uniform scalar concentration bounded by sharp edges. This suggests relatively large jumps of the scalar concentration or a large scalar gradient. This is supported by figure 4(*a–d*) where we show the norm of the scalar gradient on a two-dimensional plane across the computational domain for different Schmidt numbers. At all Schmidt numbers large scalar gradients are apparent, which are clearly concentrated in elongated regions. Similarly as in figure 2, these can be considered as the cross-sections of sheet-like structures. Note that they have a finite width and are often rolled-up at their ends. As expected the thickness of the sheets increases when Sc decreases. It is, however, remarkable that even when Sc is as small as 0.1, for which η_B is considerably larger than η, the dominating structure in the scalar gradient field is still a sheet (figure 4*d*). This observation is in agreement with the studies mentioned in the introduction, e.g. Vedula *et al.* (2001). These sheet-like structures in the scalar gradient field have been found by Holzer & Siggia (1994) who called them cliffs. We shall come back to these structures in more detail later in this paper.

The sharp cliffs give raise to a high intermittency of the scalar gradient field or alternatively of the scalar dissipation. In other studies it has been revealed that the scalar gradient field is more intermittent than the velocity gradient field (Métais & Lesieur 1992; Sreenivasan & Antonia 1997; Mydlarski & Warhaft 1998; Vedula *et al.* 2001; Brethouwer 2000). Values of the kurtosis and the skewness of the scalar dissipation rate and of fluctuations in the scalar gradient parallel to the mean gradient as obtained from our DNS are listed in table 2. The strong intermittency of the scalar

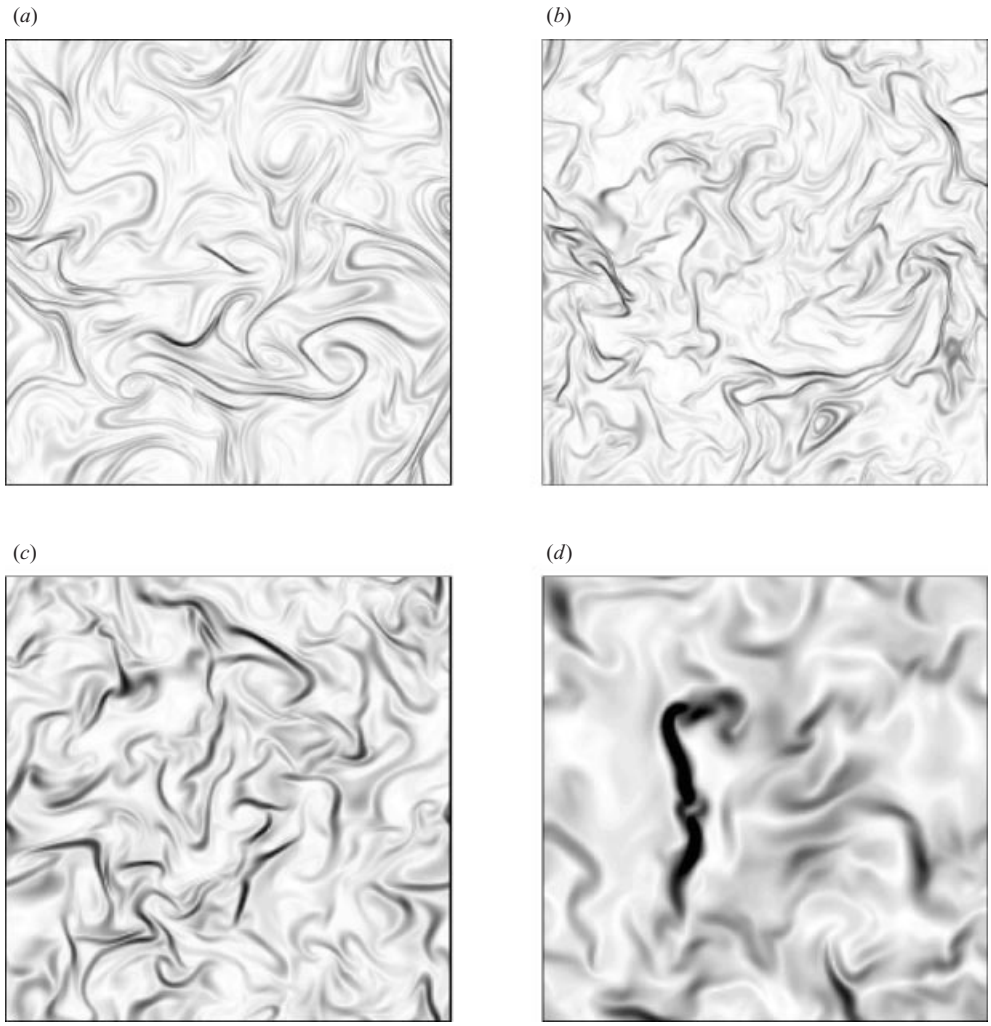

FIGURE 4. The norm of the scalar gradient on a two-dimensional plane for (*a*) run B_3 with $Sc = 25$ and $Re_\lambda = 46$, (*b*) run C with $Sc = 3$ and $Re_\lambda = 90$, (*c*) run F with $Sc = 0.7$ and $Re_\lambda = 85$ and (*d*) run D_2 with $Sc = 0.1$ and $Re_\lambda = 95$. The mean gradient is in the horizontal direction. A dark colour corresponds to a steep scalar gradient.

gradient field is reflected by the high values of the kurtosis. Even at the lowest value of Sc the kurtosis is still considerable. Consistent with other studies (Pumir 1994; Warhaft 2000), we find that the skewness of the scalar gradient parallel to the mean gradient has a non-zero value for $Sc \simeq 1$ and $Sc < 1$. At $Sc = 25$ the skewness is still non-zero. This non-zero skewness implies that the micro-structure of the scalar field is anisotropic, which, as we shall see below, is caused by a direct coupling between the small scales and the mean scalar gradient.

In order to investigate the influence of the Schmidt number on this small-scale anisotropy we show in figure 5(*a*, *b*) the probability density function (PDF) of the normalized scalar gradient parallel to the mean gradient for different Schmidt numbers. We have selected cases for which the Reynolds numbers are approximately equal, i.e. runs D_1, D_2, C with $Re_\lambda = 90$ to 95 (figure 5*a*) and runs B_1, B_2, B_3 with

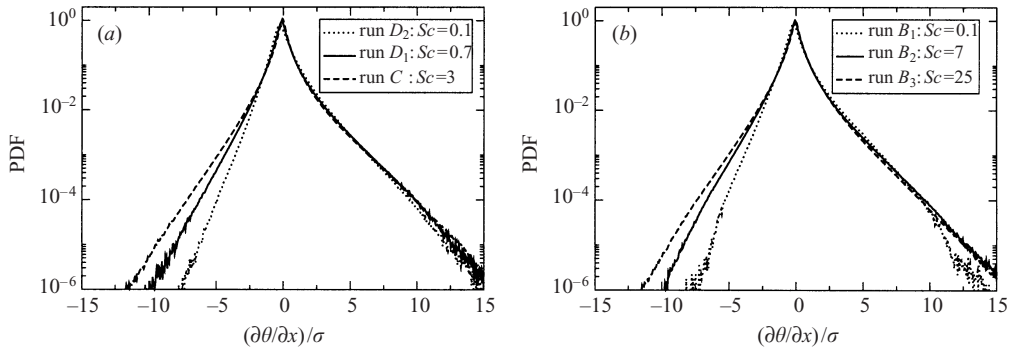

FIGURE 5. The PDF of the scalar gradient parallel to the mean gradient at (*a*) $Sc = 0.1$, 0.7, 3, and (*b*) $Sc = 1$, 7, 25. The scalar gradients are normalized by their standard deviation σ.

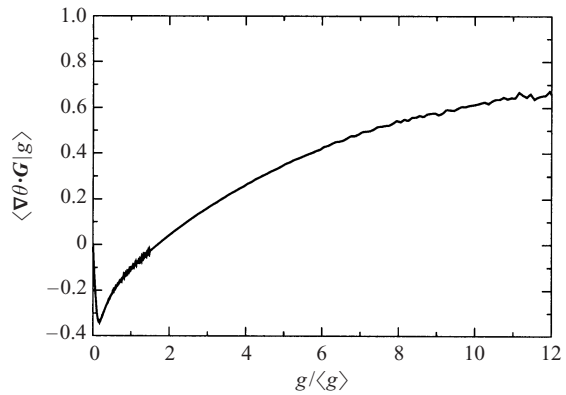

FIGURE 6. $\langle(\nabla\theta\cdot\boldsymbol{G}/(|\nabla\theta||\boldsymbol{G}|))\,|\,(g/\langle g\rangle)\rangle$: the mean value of the cosine of the angle between $\nabla\theta$ and the imposed mean gradient $\boldsymbol{G}$ conditioned on $g/\langle g\rangle$ obtained from run *F*. When the mean conditioned angle equals one the scalar gradient is aligned with the mean gradient and when it is zero the scalar gradient has an isotropic orientation.

$Re_\lambda = 46$ (figure 5*b*), so that Reynolds number effects can be neglected. The PDF for positive gradients ($\partial\theta/\partial x > 0$) does not seem to be affected by changing the Schmidt number. The probability of large negative gradients, however, increases when Sc becomes larger. Consequently, the PDF becomes more symmetric, which is consistent with the decreasing skewness shown in table 2. Combination of this result with the visualizations shown in figure 2(*a*, *b*) and figure 3 where we have seen that for $Sc \gg 1$ scalar interfaces roll up into sheets, explains why the micro-structure becomes more isotropic as the diffusivity of the scalar decreases.

Further evidence for the anisotropic distribution of the scalar gradient sheets is given in figure 6. This figure shows that especially large values of g or alternatively large scalar gradients have a preference for an orientation in the same direction as the mean gradient $\boldsymbol{G}$. However, for small values, i.e. $g/\langle g\rangle \approx 0.1$, the gradients tend to be isotropic, $\langle\nabla\theta\cdot\boldsymbol{G}|g\rangle \simeq 0$ or even tend to be opposite to the mean gradient. These results show that the sheet-like regions of steep scalar gradient or the so-called cliffs have a preferred direction normal to the mean gradient. Furthermore, we have observed that the jump in θ across the cliffs is of the order of $|\boldsymbol{G}|$ times the integral length scale ℓ for all Reynolds and Schmidt numbers, consistent with the simulations of Holzer & Siggia (1994) and Pumir (1994).

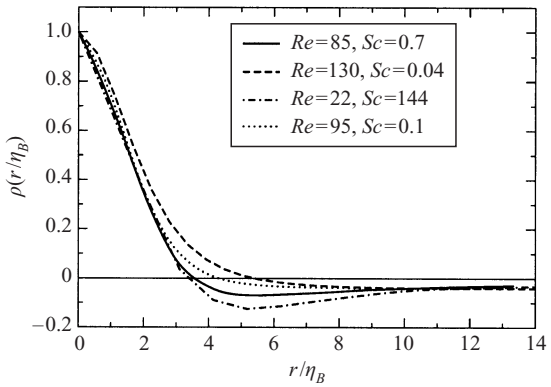

FIGURE 7. The spatial correlation function $\rho = \langle \nabla\theta(\boldsymbol{x}) \cdot \nabla\theta(\boldsymbol{x}+\boldsymbol{r})\rangle / \langle \nabla\theta \cdot \nabla\theta\rangle$. To compute this spatial correlation only points in the domain have been considered where $|\nabla\theta(\boldsymbol{x})| > 5\langle g\rangle$. The vector $\boldsymbol{r}$ is parallel to the scalar gradient at $\boldsymbol{r} = 0$, r is scaled with the Batchelor scale η_B.

Next we study the spatial dimensions of the cliffs. In figure 7 we show the correlation function $\langle \nabla\theta(\boldsymbol{x}) \cdot \nabla\theta(\boldsymbol{x}+\boldsymbol{r})\rangle / \langle \nabla\theta \cdot \nabla\theta\rangle$ with $\boldsymbol{r}$ parallel to $\nabla\theta(\boldsymbol{x})$, obtained for a large range of Reynolds and Schmidt numbers. The correlation function is conditionally determined by taking points in the computational domain where the scalar gradient is large, i.e. $g > c_{th}\langle g\rangle$ with $c_{th} = 5$, so that these points are likely to be representative for the cliffs. (The correlation function appears not to be very sensitive for the precise value of the threshold constant c_{th}.) We have normalized the spatial distance r with η_B in figure 7 (Orlandi & Antonia 2002; Brethouwer & Nieuwstadt 1999). It follows that the variation of the scaled spatial correlation function is small despite the wide range of Reynolds and Schmidt numbers. The correlation drops off very fast and is close to zero beyond $r = 4\eta_B$ for all Schmidt and Reynolds numbers. Thus $4\eta_B$ provides a reasonable estimate for the thickness of the sheets, ℓ_θ, about which there has been some uncertainty in the literature. Tong & Warhaft (1994) presented some evidence that the strain rate acting on the cliffs is proportional to u'/ℓ and therefore the thickness of the cliffs should scale with λ. Moisy *et al.* (2001) on the other hand found on the basis of experimental measurements for varying Re_λ and constant Sc that the thickness of the cliffs probably scales with η rather than with λ. This latter result is consistent with our result. Batchelor's estimate (Batchelor 1959; Tennekes & Lumley 1972) that the thickness of the scalar sheets $\ell_\theta \simeq \eta_B$ seems thus to be valid even for $Sc < 1$.

5.2. *The relation between the micro-structure of the scalar field and the structure of turbulence*

In this section we try to answer the following question: what is the influence of the turbulent structures on the formation of the cliffs that have been observed in the previous section? For this we will make use of the relations and analyses presented in § 2.

In figure 8(a, b) we present the norm of the scalar gradient g conditioned on the strain rate $s = (S_{ij}S_{ij})^{1/2}$ and conditioned on the norm of the vorticity $\omega = |\boldsymbol{\omega}|$. We see that the conditional value of g increases when the strain rate increases for all values of Sc (figure 8a). For values $Sc > 1$ this result could be expected from the analysis given in § 2 and it has also been observed by Vedula *et al.* (2001). However, the same result is also found for Sc as small as 0.04. Batchelor, Howells & Townsend (1959) have

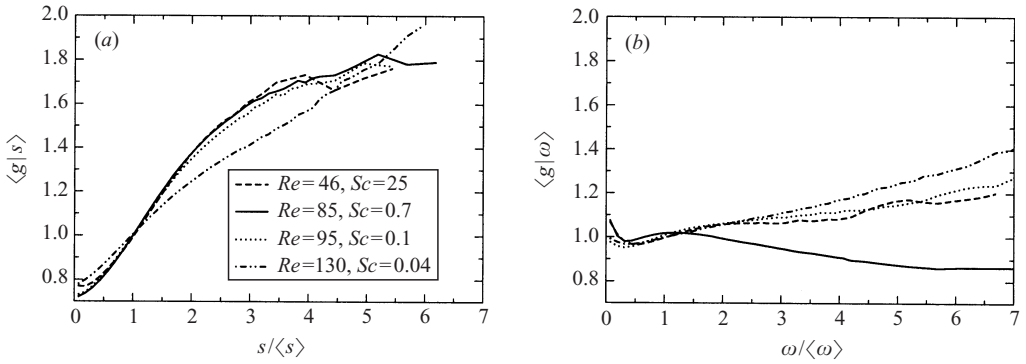

FIGURE 8. (*a*) $\langle g|s\rangle$ and (*b*) $\langle g|\omega\rangle$: the average value of the scalar gradient conditioned on the strain rate s and the vorticity ω, respectively. The statistics are obtained from runs B_3, F, D_2 and E_2. All quantities are scaled with their mean value.

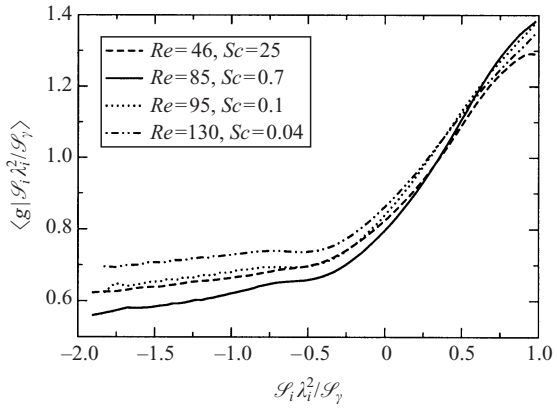

FIGURE 9. $\langle g|\mathscr{S}_i\lambda_i^2/\mathscr{S}_\gamma\rangle$: the scalar gradient conditioned on its alignment with the direction of compressive strain. The statistics are obtained from runs B_3, F, D_2 and E_2.

argued that the influence of the strain rate on the scalar gradients should disappear when $Sc < 1$ but Gibson, Ashurst & Kerstein (1988) and Kerr (1985) have observed in the results of their computations that there is still a correlation between strain rate and scalar gradients for $Sc < 1$, consistent with our observations. As argued in § 2, the vorticity does not have a direct influence on the magnitude of the scalar gradient. This agrees with the results of figure 8(*b*) where it is demonstrated that the correlation between the magnitude of the vorticity and the scalar gradient is weak and does not show a trend as a function of Sc. An equivalent result has been found by Zhou & Antonia (2000) and Pumir (1994).

In § 2 we have also seen that the amplification of scalar gradients is not only determined by the strain rate but also by the alignment between $\nabla\theta$ and the direction of compressive strain $\boldsymbol{e}_\gamma$. In figure 9 the scalar gradient conditioned on $\mathscr{S}_i\lambda_i^2/\mathscr{S}_\gamma$ is shown. This latter ratio is proportional to the alignment between $\nabla\theta$ and $\boldsymbol{e}_\gamma$ because its value becomes larger when the alignment becomes better, i.e. $\lambda_\gamma = \nabla\theta \cdot \boldsymbol{e}_\gamma/g$ approaches the value one. A negative value implies a negative production rate or reduction of the scalar gradient. According to figure 9 large scalar gradients are clearly related to high values of $\mathscr{S}_i\lambda_i^2/\mathscr{S}_\gamma$. This result is in agreement with Ashurst *et al.* (1987) who found that steep scalar gradients are aligned with $\boldsymbol{e}_\gamma$ for $Sc \sim 1$. Our

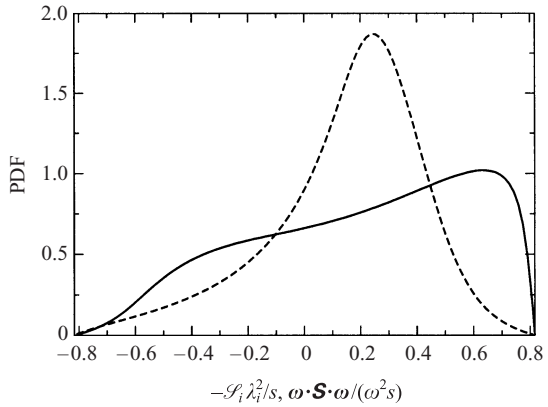

FIGURE 10. The PDFs obtained from run F of the normalized production terms of g given by $-\mathscr{S}_i\lambda_i^2/s = -\nabla\theta\cdot\boldsymbol{S}\cdot\nabla\theta/(g^2 s)$ (solid line) and of ω given by $\boldsymbol{\omega}\cdot\boldsymbol{S}\cdot\boldsymbol{\omega}/(\omega^2 s)$ (dashed line).

results, however, show that this conclusion can be extended to $Sc > 1$ and $Sc < 1$. The alignment between $\nabla\theta$ and $\boldsymbol{e}_\gamma$ for $Sc < 1$ has been also predicted by Gibson *et al.* (1988) and observed in their two-dimensional simulations.

Figure 10 presents the PDF of $\mathscr{S}_i\lambda_i^2/s = -\nabla\theta\cdot\boldsymbol{S}\cdot\nabla\theta/(g^2 s)$ with $s = (S_{ij}S_{ij})^{1/2}$. It follows that the maximal and minimal values of this ratio are $\sqrt{2/3}$ and $-\sqrt{2/3}$, respectively. These values occur when the strain tensor is given by $\mathscr{S}_\alpha : \mathscr{S}_\beta : \mathscr{S}_\gamma = 1:1:-2$ and if $\nabla\theta$ is fully aligned with $\boldsymbol{e}_\gamma$. In a turbulent flow the variations of s are large (Métais & Lesieur 1992; Brethouwer 2000; Vedula *et al.* 2001) but figure 10 shows that the variation of $\mathscr{S}_i\lambda_i^2$ normalized with s is large as well, which is a consequence of the large variation of the orientation of $\nabla\theta$ with respect to the principal axes of strain. The peak of the PDF is close to its maximal value, revealing the preferential alignment of $\nabla\theta$ with $\boldsymbol{e}_\gamma$ (Vedula *et al.* 2001) but figure 10 also shows that there is a considerable proportion of negative production. This means that in a significant part of the flow the scalar gradient $\nabla\theta$ is not aligned with the compressive strain direction but is aligned with a direction of stretching which implies a reduction of scalar gradients. In the same figure the PDF of $\boldsymbol{\omega}\cdot\boldsymbol{S}\cdot\boldsymbol{\omega}/(\omega^2 s)$ is plotted which is the normalized production rate of enstrophy (Tsinober, Ortenberg & Shtilman 1999). This ratio has its maximal value if the strain rate tensor is given by $\mathscr{S}_\alpha : \mathscr{S}_\beta : \mathscr{S}_\gamma = 2:-1:-1$ and if the vorticity is aligned with $\boldsymbol{e}_\alpha$. The figure shows that for this enstrophy production rate large positive and large negative values are more rare than for the production rate of the scalar gradient. This might provide an explanation for the larger intermittency of the scalar gradient field in comparison with the intermittency of the vorticity field (Brethouwer 2000). Moreover, the peak of the PDF is not close to the maximal value but lies at a much smaller value. The explanation for this observation is that the vorticity has the tendency to align with $\boldsymbol{e}_\beta$ (Ashurst *et al.* 1987; Ohkitani 1998), and the strain rate in the direction of $\boldsymbol{e}_\beta$ is much smaller than in the $\boldsymbol{e}_\gamma$-direction (Vedula *et al.* 2001).

After this discussion on the alignment between $\nabla\theta$ and $\boldsymbol{e}_\gamma$ we now study how this alignment is related to turbulent structures. In our discussion following (2.10) we argued that the strain itself aligns the scalar gradient with the direction of compressive strain and thus increases the normalized production rate. We also argued that vorticity or rotation of the principal axes of strain counteracts this alignment. The results of our DNS presented in figure 11(a, b) are consistent with these arguments. We observe that

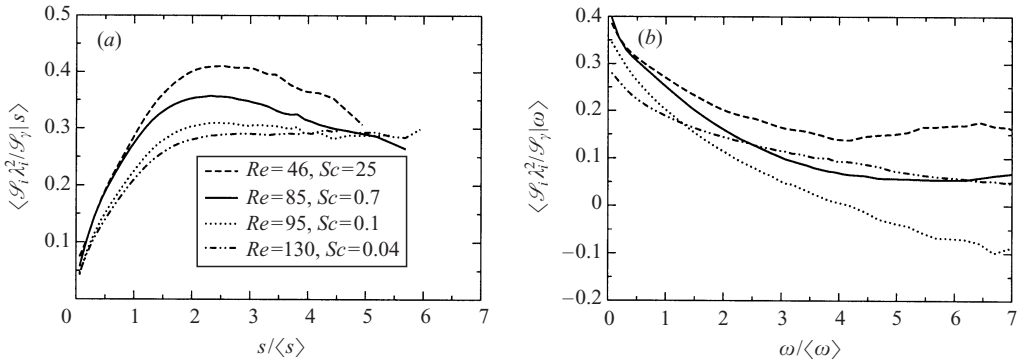

FIGURE 11. (*a*) $\langle \mathscr{S}_i\lambda_i^2/\mathscr{S}_\gamma|s\rangle$ and (*b*) $\langle \mathscr{S}_i\lambda_i^2/\mathscr{S}_\gamma|\omega\rangle$: the average values of the normalized production of g conditioned on the strain rate s and the vorticity ω, respectively. The statistics are obtained from runs B_3, F, D_2 and E_2. All quantities are scaled with their mean value.

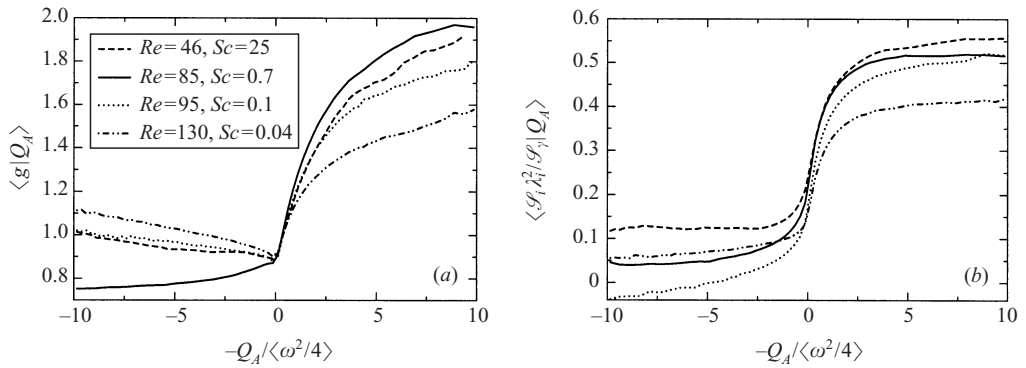

FIGURE 12. (*a*) $\langle g|Q_A\rangle$: the average value of g conditioned on the invariant Q_A, and (*b*) $\langle \mathscr{S}_i\lambda_i^2/\mathscr{S}_\gamma|Q_A\rangle$: the normalized production of g conditioned on the invariant Q_A. Here Q_A is scaled with $\langle\omega^2\rangle/4$. The statistics are obtained from runs B_3, F, D_2 and E_2.

the normalized production term increases when s increases for all Sc (figure 11*a*), at least for $s < 2\langle s\rangle$. For larger strain rates the normalized production term stays almost constant or decreases somewhat. The vorticity has an opposite effect (figure 11*b*). The normalized production term in this case increases when the vorticity decreases, with the maximal value when the vorticity is zero. The normalized production rate becomes very small at large values of the vorticity. Furthermore, we observe that the influence of the strain rate and the vorticity are quite similar for all values of Sc.

The interpretation of the results given above is that the probability of alignment of $\nabla\theta$ with $\boldsymbol{e}_\gamma$ is high if the strain rate is large and the vorticity is small. This can be illustrated further with help of the invariants of the velocity gradient tensor which have been discussed in § 3, and which allow us to study in more detail the connection between the turbulence and the topology of the scalar micro-structure.

The effect of straining and vorticity is confirmed by figure 12(*a*, *b*) where we present the normalized production rate of the scalar gradient and the scalar gradient itself conditioned on the invariant Q_A of the velocity gradient tensor. When the vorticity is larger than the strain rate, so that $-Q_A < 0$, the normalized production rate is very small (figure 12*b*). In the opposite case, when the strain dominates and $-Q_A > 0$, the normalized production increases with increasing values of Q_A. The same conclusions

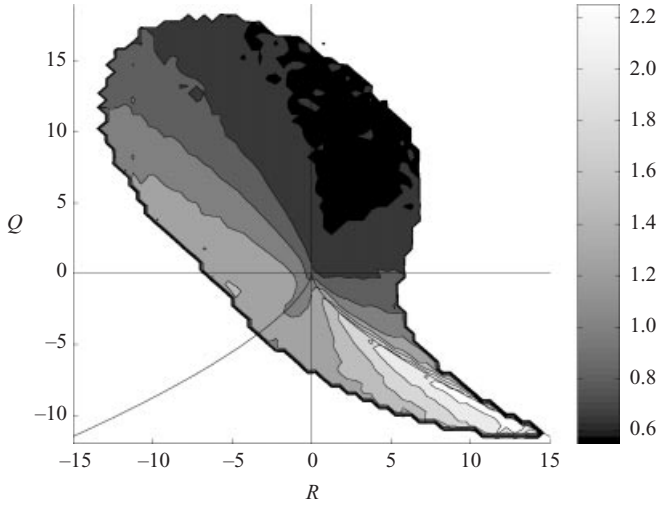

FIGURE 13. $\langle g|Q_A, R_A\rangle$: the mean value of the scalar gradient g conditioned on the invariant Q_A and R_A obtained from run F. The scalar gradient is scaled with its mean value and the invariants Q_A and R_A with $(\frac{1}{2}\omega)^2$ and $(\frac{1}{2}\omega)^3$, respectively.

apply to the scalar gradient (figure 12a) where we also see a clear difference between $Q_A > 0$ and $Q_A < 0$. In this case we see again the same trends independent of the values of Sc, which implies that vorticity and strain rate have a similar influence on the micro-structure of the scalar field for small and large Sc.

Next we show in figure 13 the scalar gradient conditioned on Q_A and R_A as obtained from our DNS results. The value of the conditioned scalar gradient is indicated by the shades of grey. In the white region outside the pear-shaped contour the number of samples is too small to determine an accurate value of the conditioned scalar gradient. In agreement with figure 12(a) we see that the mean value of g is small for positive Q_A (vorticity dominated) and large for negative Q_A (strain dominated). More precisely, we observe with help of figure 1 that in regions with a stable focus/stretching topology and positive Q_A and in regions with an unstable focus/contracting topology the $g/\langle g\rangle$ is on average smaller than one. The smallest conditional values of g appear in regions with an unstable focus/contracting topology. Large conditional values of g can be found in regions with an unstable node/saddle/saddle topology, in particular at the points with large negative values of Q_A, $R_A > 0$ and $D < 0$ and at the points close to the tent-like curve $D = 0$. This means that the steepest scalar gradients can be found in regions that are strongly dominated by a strain with one direction of compression and two directions of stretching.

Let us now turn to the alignment properties and the production rate of scalar gradients in terms of the invariants Q_A and R_A to investigate why the steepest scalar gradients are formed in regions with an unstable node/saddle/saddle topology. Figure 14 presents the scalar gradient production rate $-\mathscr{S}_i\lambda_i^2$ normalized with $s = (S_{ij}S_{ij})^{1/2}$ and conditioned on Q_A and R_A. We observe that negative conditional values of the scalar gradient production rate are found in regions with either a stable focus/stretching or an unstable focus/contracting topology. The largest negative conditional values are found in regions with a positive Q_A (vorticity dominated) and an unstable focus/contracting topology. In these regions scalar gradients are reduced by strain because of alignment of the scalar gradient with a direction of

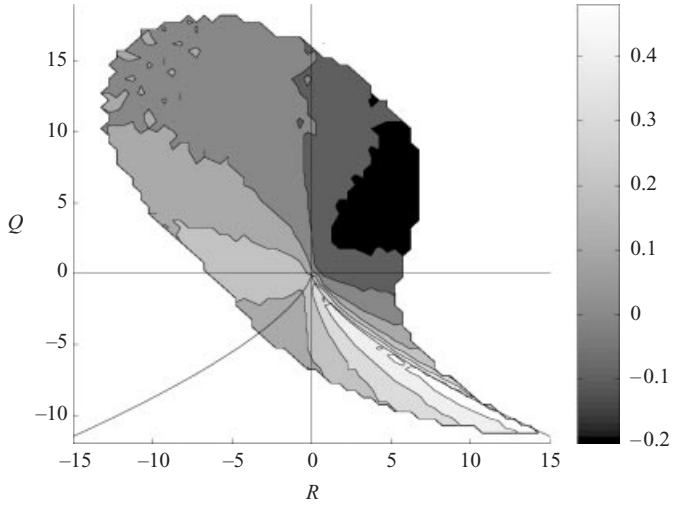

FIGURE 14. $\langle -\mathscr{S}_i\lambda_i^2/s|Q_A, R_A\rangle$: the mean value of normalized production rate of g conditioned on the invariant Q_A and R_A obtained from run F. The scalar gradient is scaled with its mean value and the invariants Q_A and R_A with $(\frac{1}{2}\omega)^2$ and $(\frac{1}{2}\omega)^3$, respectively.

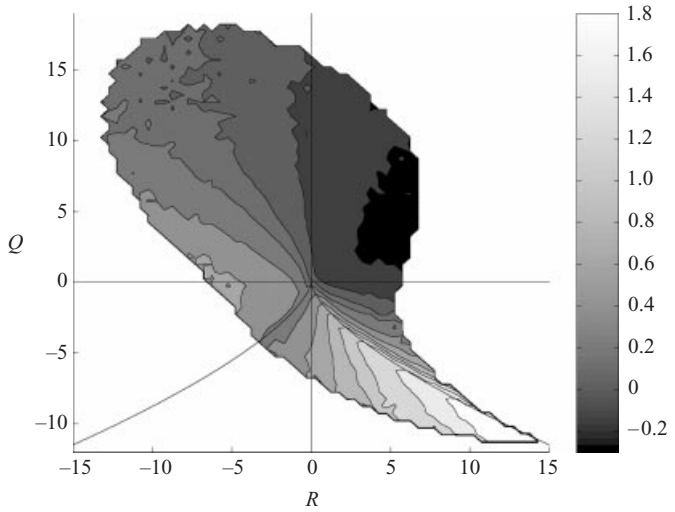

FIGURE 15. $\langle -\mathscr{S}_i\lambda_i^2|Q_A, R_A\rangle$: the mean value of the production rate of g conditioned on the invariant Q_A and R_A obtained from run F. The scalar gradient is scaled with its mean value, the production rate is scaled with the mean strain rate and the invariants Q_A and R_A with $(\frac{1}{2}\omega)^2$ and $(\frac{1}{2}\omega)^3$, respectively.

stretching, which can be either $\boldsymbol{e}_\alpha$ or $\boldsymbol{e}_\beta$ if $\mathscr{S}_\beta > 0$. The scalar gradient shows the best alignment with the direction of compressive strain at the points with large negative values of Q_A, $R_A > 0$ and $D < 0$, especially at points that are close to the tent-like $D = 0$ curve. At the same points figure 15 shows the highest averaged production rate of scalar gradients because of a combination of a large strain rate and a good alignment between $\nabla\theta$ and $\boldsymbol{e}_\gamma$. This leads to the formation of large scalar gradients as observed in figure 13. Production rates are, however, significantly lower in regions with with either a stable focus/stretching or an unstable

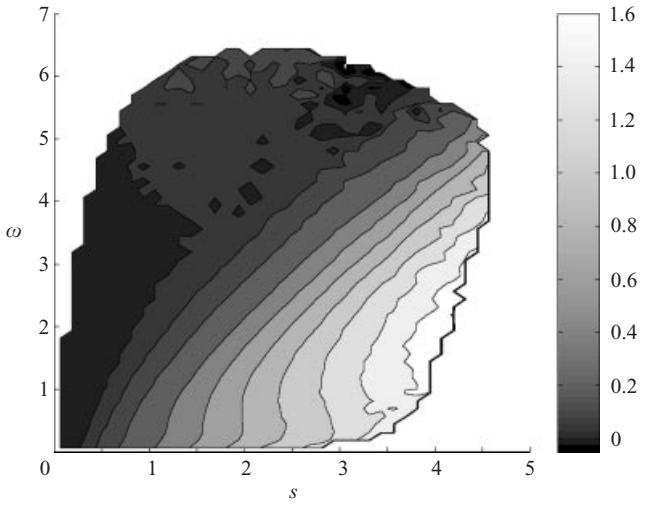

FIGURE 16. $\langle -\mathscr{S}_i\lambda_i^2|s,\omega\rangle$: the mean value of the production rate of g conditioned on the strain rate s and the vorticity ω obtained from run F. The scalar gradient, strain rate and vorticity are scaled with their mean values, the production rate is scaled with the mean strain rate.

focus/contracting topology and are even negative in regions where Q_A and R_A are positive.

Figure 16 shows the production rate of scalar gradients conditioned on the strain rate and the vorticity. The influence of the vorticity on the scalar gradient production rate is rather large as we can observe in figure 16. We see that the production rate increases when for constant vorticity the strain rate increases. On the other hand the production rate decreases when for constant strain rate the vorticity increases. This latter occurs because the alignment of the scalar gradient with the direction of compressive strain is destroyed when the vorticity increases. On the whole the production rate is small for a high vorticity, even for a strain rate much larger than its average value.

Our simulations prove that straining motions play an important role in the generation of steep scalar gradients or cliffs which, as we have seen, have a preferential orientation perpendicular to the mean scalar gradient. According to the visualizations of Holzer & Siggia (1994) it seems that the direction of contraction of the straining motions is along the mean gradient during the formation of the cliffs. This observation is supported by figure 17 where we show the absolute value of the cosine of the angle between $\boldsymbol{e}_\gamma$ and the mean gradient $\boldsymbol{G}$ conditioned on g. This result should not be interpreted as that the strain rate itself is anisotropic. Namely, the result for the mean unconditional value $\langle|\boldsymbol{e}_\gamma\cdot\boldsymbol{G}|\rangle/|\boldsymbol{G}|$, i.e. the absolute value of the cosine of the angle between $\boldsymbol{e}_\gamma$ and the mean gradient $\boldsymbol{G}$, is found to be equal to 0.500 which implies a perfect isotropic orientation of the compressive strain direction. Figure 17 shows that at the places in the scalar field where the scalar gradients are steep, the compressive strain direction and the mean gradient more or less coincide. This means that a significant part of the steep scalar gradients or the cliffs is formed by those straining motions, the direction of contraction of which is along the mean gradient.

Figure 18 presents the scalar gradient production rate conditioned on the cosine of the angle between $\nabla\theta$ and the mean gradient. We see that the production rate increases considerably when the alignment between $\nabla\theta$ and the mean gradient increases. The

Run	G			F		
Re_λ	59	59	59	85	85	85
Sc	0.7	0.7	0.7	0.7	0.7	0.7
Direction	x_1	x_2	x_3	x_1	x_2	x_3
Amplification	0.368	0.277	0.291	0.369	0.299	0.304
Rotation	−0.0187	0.0123	0.0063	−0.0126	0.0012	0.0114
Mean gradient	0.0120	0.0259	0.0260	0.0054	0.0106	0.0112
Total production	0.361	0.316	0.323	0.362	0.311	0.327

TABLE 3. The average values of the first three terms, i.e. the amplification, the rotation and the mean gradient term, on the right-hand side of the equation for g_ℓ^2 (2.6) obtained from two simulations. When the direction is x_1 the scalar gradient $\partial\theta/\partial x_\ell$ is parallel to the mean gradient, otherwise it is normal to the mean gradient. The total production (last row of the table) is the sum of all three terms, i.e. amplification, rotation and the mean gradient term. All the terms are scaled with the sum of all three terms in all three directions.

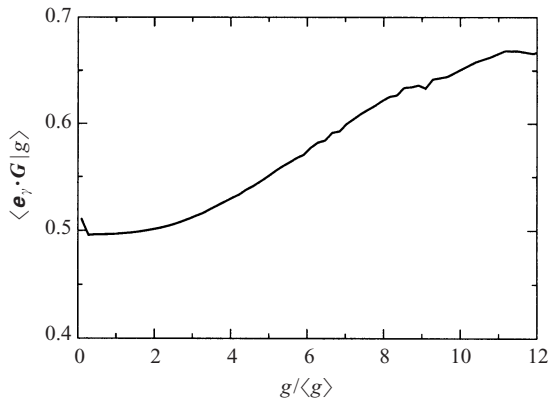

FIGURE 17. $\langle (|\boldsymbol{e}_\gamma \cdot \boldsymbol{G}|/|\boldsymbol{G}|) \,|\, (g/\langle g \rangle) \rangle$: the mean value of the cosine of the angle between the direction of compressive strain $\boldsymbol{e}_\gamma$ and the imposed mean gradient $\boldsymbol{G}$ conditioned on $g/\langle g \rangle$. In case there is no preferential alignment between $\boldsymbol{e}_\gamma$ and $\boldsymbol{G}$ the conditional value equals a half.

anisotropy that is observed in the moments of the scalar gradients is thus even more strongly present in the correlation of the scalar gradient with the velocity gradient. Additional data are given in table 3. The average values of the amplification term, the rotation term and the mean gradient term on the right-hand side of equation (2.6) for g_ℓ^2, are presented for all three directions in the same table. Here, x_1 is here parallel and x_2 and x_3 are normal to the mean scalar gradient. The difference between the terms computed for the x_2- and the x_3-directions is a consequence of statistical uncertainty, so that the values can be considered as being equal. The table shows that the amplification term is much larger than the mean gradient term and the rotation term because the scalar gradient is mainly normal to the vorticity (Pumir 1994). Also, we see that the amplification term is larger for the x_1- than for the x_2- and x_3-directions in agreement with figure 17. The statistics of the rotation term are not well-converged, reflected by the large difference between the rotation term for the x_2- and the x_3-directions. It seems, however, that it redistributes scalar gradient fluctuations parallel to the mean scalar gradient to the directions normal to this gradient. The relative importance of the mean gradient term decreases with increasing Reynolds number, although the range of Reynolds numbers is rather limited. Nevertheless, this is in

T/T_e	$\Delta t/\tau$	h/τ	T_L/τ	T_L/T_e	$\mathscr{T}_\epsilon/T_L$	$\mathscr{T}_{\omega^2}/T_L$	$\mathscr{T}_\epsilon/\tau$	$\mathscr{T}_{\omega^2}/\tau$	$\mathscr{T}_\theta/T_L$	$\mathscr{T}_\chi/T_L$	$\mathscr{T}_\chi/\tau$
12.0	0.017	0.20	9.34	0.728	0.458	0.757	4.28	7.06	2.08	0.370	3.46

TABLE 4. Lagrangian time scales of the flow and the scalar. T/T_e: the duration of the run in terms of the eddy-turnover time T_e; τ: the Kolmogorov time scale; Δt: the time step of the time integration; h: the time interval of sampling of the Lagrangian statistics; T_L: Lagrangian integral time scale of the velocity; $\mathscr{T}_\varepsilon$: integral time scale of ϵ; $\mathscr{T}_{\omega^2}$: integral time scale of the enstrophy ω^2; $\mathscr{T}_\theta$: integral time scale of the scalar concentration; $\mathscr{T}_\chi$: integral time scale of the scalar dissipation rate.

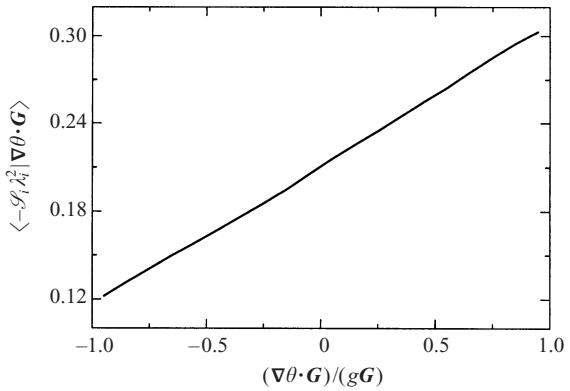

FIGURE 18. $\langle -\mathscr{S}_i\lambda_i^2 \,|\, \nabla\theta\cdot\boldsymbol{G}/(g|\boldsymbol{G}|)\rangle$: the mean value of the production term of g conditioned on the cosine of the angle between the scalar gradient and the imposed mean gradient. The statistics are obtained from run F.

agreement with the arguments given in § 2 and with the results of Vedula *et al.* (2001). Moreover, the mean gradient term for the x_1-direction is about half that for the x_2- and the x_3-directions. We see thus that the rotation and the mean gradient term partly compensate the anisotropy of the amplification term. Consequently, the total production, i.e. the sum of the amplification, rotation and the mean gradient term, is more isotropic than the amplification term alone. Nonetheless, the total production for the direction parallel to the mean scalar gradient remains larger than the total production for the direction normal to the mean gradient with an anisotropy quite similar for the two Reynolds numbers. It would be interesting to see if this extends to a wider range of Reynolds numbers.

5.3. *Lagrangian statistics of mixing*

Fung & Vassilicos (1998) have observed that particle pairs separate very rapidly in straining regions. Here we have observed that straining regions are also very important for the mixing process because they lead to a rapid formation of cliffs. Cliff formation occurs when two particles with different concentrations are brought close together. These seemingly opposite results are nevertheless consistent because in the saddle-point topology of the velocity field in which cliffs are formed, particles first approach each other before they separate quickly. The concept of rapid cliff formation in straining regions is tested here by tracking 27 000 fluid particles in run F ($Sc = 0.7$ and $Re_\lambda = 85$). The Lagrangian time scales obtained from this run are listed in table 4.

To obtain a first impression of the mixing and the related turbulence processes in a Lagrangian frame we have plotted in figure 19 time series of the norm of the vorticity, the strain rate and the scalar gradient observed along the path of a fluid

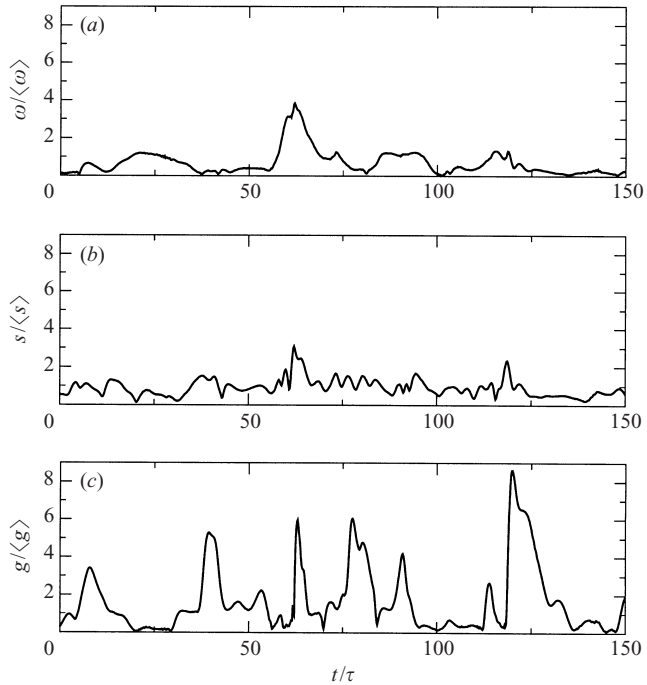

FIGURE 19. Time series of (*a*) the vorticity, (*b*) strain and (*c*) scalar gradient.

particle. The time is normalized with the Kolmogorov time scale. The time series show that the vorticity, strain rate and the scalar gradient are very intermittent. Moreover, figure 19 also suggests that the scalar gradient is more intermittent than the vorticity and the strain rate. Lagrangian auto-correlation functions obtained from DNS show that the correlation time of the scalar dissipation rate is shorter than the correlation time of the kinetic energy dissipation and the enstrophy (Brethouwer 2000; Yeung 2001). The time series of the scalar gradient g show short events of very large values, implying steep gradients or rapid molecular mixing. The duration of these events is at most a few Kolmogorov time scales. For instance, at $t/\tau = 120$ we see a sudden strong increase of the scalar gradient with a peak value several times the mean value, after which the gradient decreases again very rapidly.

Let us study these extreme events in more detail. For this purpose, we define an ensemble of events. In the Lagrangian time series for the 27 000 fluid particles we define an event when the instantaneous scalar gradient exceeds the mean gradient $\langle g\rangle$ by a given threshold. Each event is labelled by the time instant at which the scalar gradient g reaches its maximum value and this moment is considered to be the point of reference where we set $t = 0$. We then compute the scalar and velocity parameters in the short period of time before and after $t = 0$. Finally, we calculate the ensemble average of all detected events with each event centred at $t = 0$. For the value of the threshold we have taken either 4 or 6 times the mean value $\langle g\rangle$. For $g \geqslant 4\langle g\rangle$ we have detected 16 262 events during the entire simulation period. In this case the number of events detected per particle and per eddy-turnover time T_e is on average 0.07 which corresponds to 0.10 detected events per integral time scale T_L. In the following figures we present the ensemble-averaged results for both threshold values in order to show the trend of the statistics if we consider more extreme events.

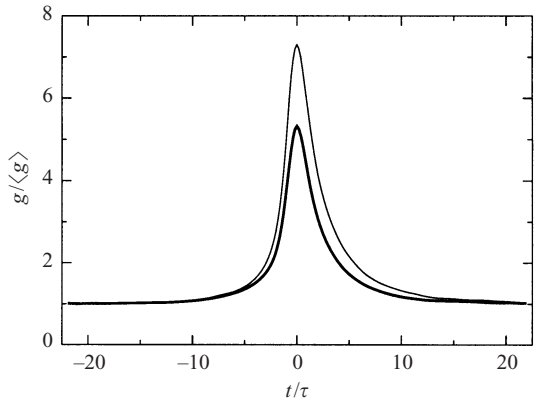

FIGURE 20. The time evolution of g in a short period of time before and after it reaches a high value. The time is normalized with the Kolmogorov time scale τ and g with its mean value. This time evolution is an ensemble average of all events which satisfy $g \geqslant 4\langle g\rangle$ (the thick line) or $g \geqslant 6\langle g\rangle$ (the thinner line).

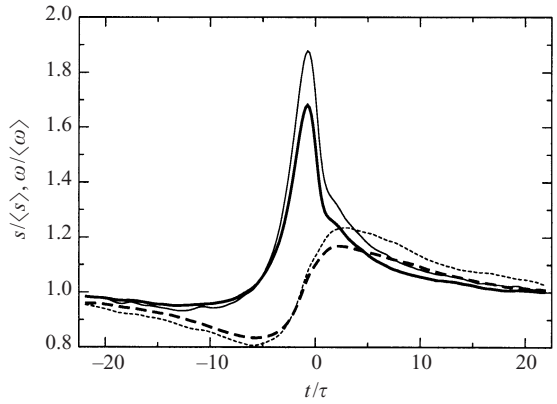

FIGURE 21. The time evolution of $s = (S_{ij}S_{ij})^{1/2}$ (solid line) and $\omega = |\boldsymbol{\omega}|$ (dashed line) before and after g reaches its highest value at $t = 0$. The time is normalized with the Kolmogorov time scale and s and ω with their mean value. This time evolution is an ensemble average of all events which satisfy $g \geqslant 4\langle g\rangle$ (the thick lines) or $g \geqslant 6\langle g\rangle$ (the thinner lines).

In figure 20 we present the Lagrangian evolution of the ensemble-averaged norm of the scalar gradient normalized by its mean value. The figure shows a cycle in which the gradient grows within a few Kolmogorov time scales to a maximum which is larger than the mean value by several factors, after which it decreases again to a value close to the mean, i.e. $g/\langle g\rangle \simeq 1$. It is also interesting to investigate the evolution of the strain rate and the norm of the vorticity during the detected events. These are presented in figure 21 where the absolute value of the strain rate and the vorticity are shown, both normalized with their mean values. Here $t = 0$ is again the time instant when g reaches its maximum value. Similar to the scalar gradient the strain rate shows also a short moment of a relatively high value. The strain rate peaks slightly before $t = 0$. Figure 21 shows that the strain rate increases by a factor of 1.7 to 1.9, which is considerably smaller than the factor of 5 to 7 which we found for g. The Lagrangian evolution of the vorticity is quite different. Figure 21 shows that after a slight decrease the vorticity starts to increase around $t = -5\tau$. The relative increase

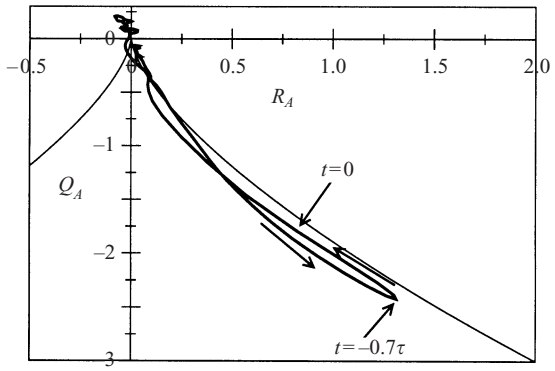

FIGURE 22. The ensemble-averaged trajectory in the (R_A, Q_A)-plane during the event where $g > 6\langle g \rangle$, at $t = 0$ (shown with the arrow in the plot) the scalar gradient has its maximal value.

of the vorticity is, however, much smaller than the increase of the strain rate and the scalar gradient. In the neighbourhood of $t = 0$ the strain rate is much larger than the vorticity, implying that the fluid particles are in a strain-dominated region, i.e. $Q_A < 0$. This is confirmed by figure 22 which shows the ensemble-averaged trajectory in the (R_A, Q_A)-plane during the period when g becomes large. The trajectory starts near the origin of the (R_A, Q_A) plot and just before $t = 0$ it moves down quickly along the $D = 0$ line. After $t = 0$ the trajectory returns again to the origin. The steep scalar gradients are thus formed by turbulent structures with a short lifetime and with an unstable node/saddle/saddle topology.

Next we investigate the Lagrangian evolution of the production rate of the scalar gradient, normalized with its maximal value and unnormalized. This is shown in figure 23(a, b). Recalling figure 11 we know that the mean normalized production rate increases when the strain increases but decreases when the vorticity increases. Because the strain rate increases considerably before $t = 0$ while for the same fluid element the vorticity hardly changes, we expect a strong increase of the normalized production rate. This is consistent with figure 23(a). Just before $t = 0$ the normalized production rapidly increases, which implies that the scalar gradient rapidly rotates to the direction of the compressive strain. After $t = 0$ the production very rapidly decreases again. The maximum value reached by the normalized production rate is about 0.75, showing that the scalar gradient is close to being completely aligned with the direction of the compressive strain at $t = 0$. The combined effects of increasing strain rate and rotation of $\nabla\theta$ to the direction of compressive strain result in a large increase of the production term of the scalar gradient, $-g\mathscr{S}_i\lambda_i^2$ as shown by figure 23(b). This result confirms our argument presented in § 2 that the production rate of the scalar gradient is a nonlinear function of the strain rate.

As we have already seen, the presence of a mean gradient has a direct influence on the generation of steep scalar gradients because a significant part of the steep scalar gradients is generated by a convergence of the flow along the mean gradient. In figure 24(a) the Lagrangian evolution of the absolute value of the cosine of the angle between $\boldsymbol{e}_\gamma$ and the mean gradient is presented during the period when g reaches a high value. When $t < -15\tau$ and $t > 15\tau$ the averaged value of the angle is around 0.5 which means that the orientation of $\boldsymbol{e}_\gamma$ has an isotropic distribution. However, just before $t = 0$ the average value of the angle shows a peak. This peak is small for the events with $g > 4\langle g \rangle$ but it becomes considerable for the events with

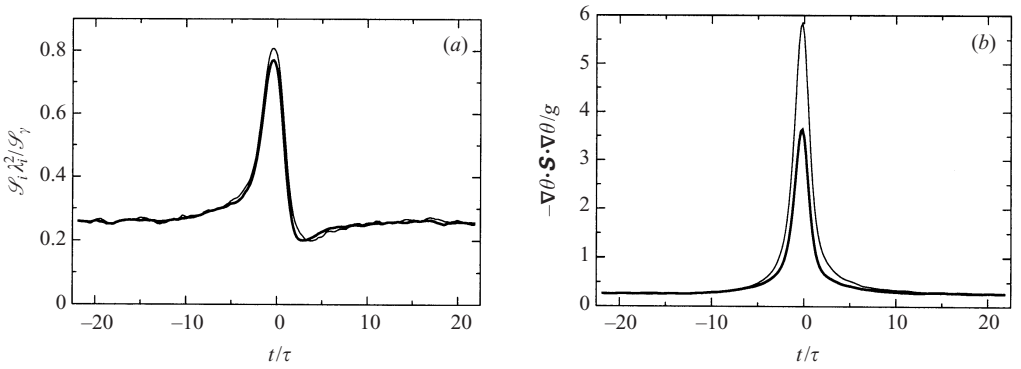

FIGURE 23. The time evolution of (a) the normalized production rate of g given by $\mathscr{S}_i\lambda_i^2/\mathscr{S}_\gamma$, and ($b$) the production term $-g\mathscr{S}_i\lambda_i^2$ before and after g reaches a highest value at $t = 0$. The time is normalized with the Kolmogorov time scale. This time evolution is an ensemble average of all events which satisfy $g \geqslant 4\langle g\rangle$ (the thick lines) or $g \geqslant 6\langle g\rangle$ (the thinner lines).

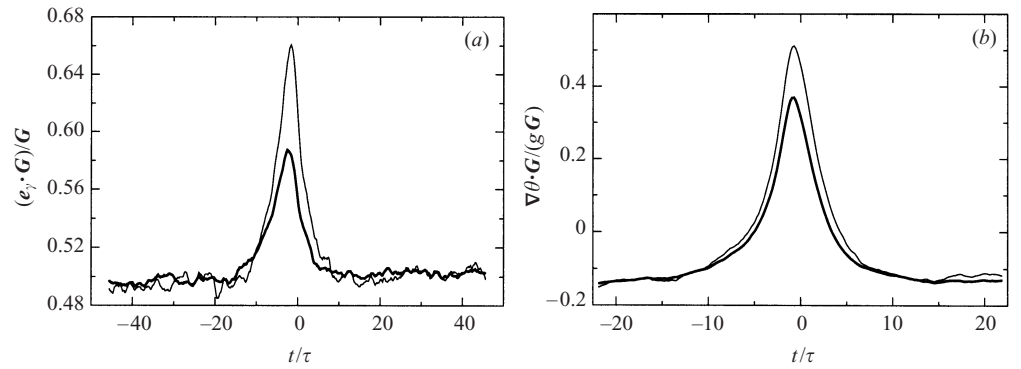

FIGURE 24. The time evolution of (a) the alignment between $\boldsymbol{e}_\gamma$ and the mean gradient $|\boldsymbol{e}_\gamma\cdot\boldsymbol{G}|/|\boldsymbol{G}|$, and ($b$) the alignment between $\nabla\theta$ and the mean gradient $(\nabla\theta\cdot\boldsymbol{G})/(g|\boldsymbol{G}|)$ before and after g reaches a high value. At $t = 0$, g has its peak value. The time is normalized with the Kolmogorov time scale. This time evolution is an ensemble average of all events which satisfy $g \geqslant 4\langle g\rangle$ (the thick lines) or $g \geqslant 6\langle g\rangle$ (the thinner lines).

$g > 6\langle g\rangle$. Thus at least in a part of the recorded events the formation of the steep scalar gradients is a consequence of a convergence of the flow field approximately along the mean gradient. This implies the direct production of a small-scale gradient where molecular mixing is dominant, from the mean gradient without intervention of a cascade process. This direct relation between $\nabla\theta$ and $\boldsymbol{G}$ is further illustrated in figure 24(b).

Because of the rotation of $\nabla\theta$ to the mean gradient and the additional alignment between $\nabla\theta$ and $\boldsymbol{e}_\gamma$ we can expect that the second and third terms on right-hand side of (2.5), which are related to the mean gradient, will increase. In figure 25 the Lagrangian evolution of these terms is shown. Both these terms indeed show a peak. However, if we compare the magnitude of these production terms with the peak value of the first term on the right-hand side of (2.5) shown in figure as 23(b), we can conclude that their contribution to the creation of scalar gradients is insignificant. This result was already predicted in § 2 and it has also been observed by Vedula *et al.* (2001).

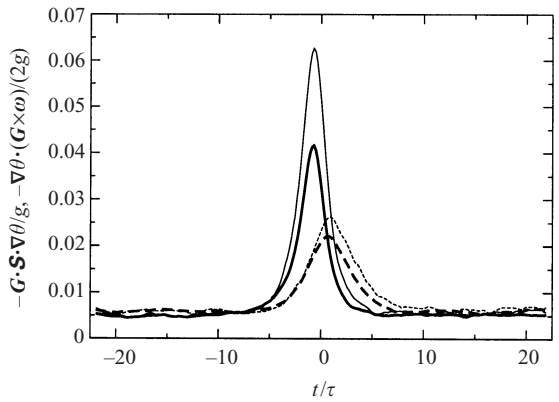

FIGURE 25. The time evolution of the production terms $-\boldsymbol{G}\cdot\boldsymbol{S}\cdot\nabla\theta/g$ (solid lines) and $-\nabla\theta\cdot(\boldsymbol{G}\times\boldsymbol{\omega})/g$ (dashed lines) before and after g reaches a highest value at $t = 0$. The time is normalized with the Kolmogorov time scale. This time evolution is an ensemble average of all events which satisfy $g \geqslant 4\langle g\rangle$ (the thick lines) or $g \geqslant 6\langle g\rangle$ (the thinner lines).

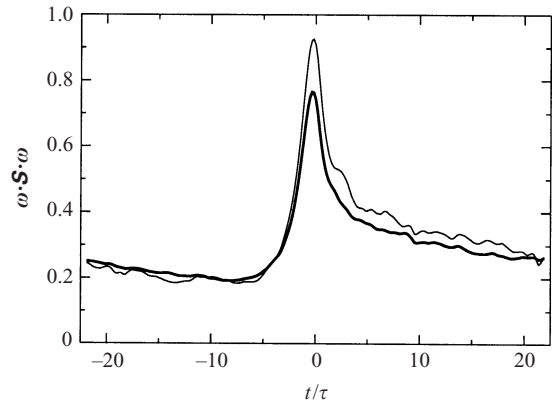

FIGURE 26. The production rate of the enstrophy $\boldsymbol{\omega}\cdot\boldsymbol{S}\cdot\boldsymbol{\omega}$ before and after g reaches a highest value at $t = 0$. The time is normalized with the Kolmogorov time scale. This time evolution is an ensemble average of all events which satisfy $g \geqslant 4\langle g\rangle$ (the thick line) or $g \geqslant 6\langle g\rangle$ (the thinner line).

Tsinober *et al.* (1999) have demonstrated that regions dominated by strain are also regions of the strongest interaction between vorticity and strain. In figure 26 the ensemble average of the production rate of enstrophy, i.e. $\boldsymbol{\omega}\cdot\boldsymbol{S}\cdot\boldsymbol{\omega}$, is presented. We observe that this production rate shows a peak at about the same time that the production rate of g has a peak. This implies that the vorticity vector experiences stretching at $t = 0$ and it follows thus that the development of steep scalar gradient sheets coincides with an increased interaction between the strain rate and the vorticity.

Finally, we present in figure 27 a Lagrangian time series of $\nabla\theta\cdot\boldsymbol{\omega}$ and its norm $g\,\omega$. In § 2 we have argued that the variation of $\nabla\theta\cdot\boldsymbol{\omega}$ will be small in comparison with the variation of its norm $g\,\omega$. This is confirmed by the computed Lagrangian time series, shown in figure 27. The fluctuations in $\nabla\theta\cdot\boldsymbol{\omega}$ are indeed very small in comparison with the fluctuations of $g\,\omega$. A small value of $\nabla\theta\cdot\boldsymbol{\omega}$ when $g\,\omega$ is large implies that $\nabla\theta$ and $\boldsymbol{\omega}$ are nearly perpendicular to each other at the instant when both the vorticity and the scalar gradient are amplified by strain. Other time series of $\nabla\theta\cdot\boldsymbol{\omega}$ and of $g\,\omega$ that we have computed show a similar behaviour. It means that the stretching of the

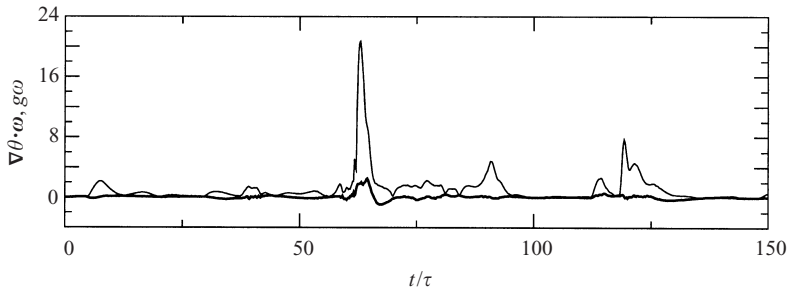

FIGURE 27. Time series of $\nabla\theta\cdot\boldsymbol{\omega}/(\langle g\rangle\langle\omega\rangle)$ (thick line) and of $g\omega/(\langle g\rangle\langle\omega\rangle)$ (thin line).

vorticity and the amplification of the scalar gradient by strain happens in directions perpendicular to each other as argued in § 2. It is thus likely that the generation of the scalar gradient sheet is accompanied by the generation of a weak vortex sheet with the vorticity vector lying in the plane of the sheet. The subsequent roll-up of this sheet into a vortex is then the next step. This process may lead to the strong vortices which have been identified in simulations by Jiménez *et al.* (1993) and which have been called 'worms'.

6. Conclusion

By means of direct numerical simulations of isotropic turbulence together with a scalar with a linear mean gradient, we have studied the micro-scales of the scalar fluctuation field in terms of the structures of the turbulence velocity field and of the Eulerian and Lagrangian statistics for a wide range of Schmidt numbers. First, we have reviewed in § 2 the well-established concepts about turbulent straining in combination with vortex stretching and roll-up and their effect on the scalar field. This leads to a picture of the generation of steep scalar gradients or cliffs by strong and short-lived straining deformations. The deformation tensor in this case has only one negative or compressive eigenvalue and two positive or expansive eigenvalues so that scalar cliffs are deformed into thin sheet-like structures which can be relatively flat or folded.

In view of the three questions formulated at the end of the introduction, we state the following conclusions.

(i) Visualizations of our simulation data confirm the existence of spatially intermittent sheet-like structures of the scalar gradient field and we have found that these occur for the whole range of the Schmidt numbers between $0.04 < Sc < 144$. Conditional statistics demonstrate that over the full range of Reynolds and Schmidt numbers of our simulations the steepest scalar gradients are preferentially aligned with the imposed mean scalar gradient. This implies that the micro-structure of the scalar field is directly influenced by the large-scale mean concentration gradient and this leads to a small-scale anisotropy. Other studies show that this direct coupling between micro- and macro-scales persists at larger Reynolds numbers than those that we have considered here (Hunt *et al.* 1988; Vedula *et al.* 2001; Mydlarski & Warhaft 1998). Furthermore, we have observed that the scalar gradient–velocity gradient correlation is influenced by the mean scalar gradient.

(ii) The structures with large scalar gradient are created in a strain-dominated region which persists for a short period of the order of several Kolmogorov time scales. The result is a sheet-like structure. The thickness of the sheet is of the order of

the Batchelor scale. The direct coupling with large scales causes the straining regions to have lateral dimensions considerably larger than the Kolmogorov scale. The scalar gradients are relatively weak in vorticity-dominated regions because in these regions the scalar gradients experience much less stretching than in strain-dominated regions due to misalignment between the scalar gradient and the direction of the compressive strain. Scalar gradients can even be reduced in vorticity-dominated regions.

(iii) Based on Lagrangian statistics taken along trajectories of fluid particles, we found that the extreme events that generate steep scalar cliffs coincide with strong straining motions. Because the jumps of the scalar across these cliffs are of the order of the integral length scale times the mean scalar gradient, we argue that the large-scale straining motions have an unstable node/saddle/saddle topology of the velocity field. This is confirmed by an analysis based on the invariants of the velocity gradient tensor. In such a velocity field the separation between fluid particles reduces very rapidly from being proportional to the integral length scale to the order of the Batchelor length scale after which particles again separate. This confirms the physical validity of the Lagrangian stochastic two-particle models where mixing occurs only when particle pairs meet due to strain.

The rapid generation of cliffs is accompanied by an increased production rate of enstrophy. Although the increase of vorticity is relative small our simulations suggest that the same straining motions that generate the cliffs also form weak vortex sheets. These vortex sheets are unstable and roll up as shown by Kevlahan & Hunt (1997) leading to concentrated vortex tubes. Our visualizations at large Schmidt numbers suggest that these vortex tubes then cause a roll-up of the scalar gradient sheets. Such roll-up does not occur at Schmidt numbers $\leqslant 1$.

Most of the molecular mixing takes place in these sheet-like cliffs of strong gradients. In addition we have found that the mixing events in the Lagrangian frame are strongly intermittent, consistent with the Eulerian view.

We gratefully acknowledge T. Dubois for providing his numerical code. We also wish to thank A. R. Kerstein, A. Tsinober and P. K. Yeung for their advice and help, and J. Soria for giving us figure 1. The valuable comments by the referees are highly appreciated. Computer time was made available by the National Computing Facilities Foundation (NCF). This work has been financially supported by the Netherlands Foundation for Fundamental Research on Matter (FOM).

REFERENCES

Ashurst, W. T., Kerstein, A. R., Kerr, R. M. & Gibson, C. H. 1987 Alignment of vorticity and scalar gradient with strain rate in simulated Navier–Stokes turbulence. *Phys. Fluids* **30**, 2343–2353.

Balachandar, S. & Maxey, M. R. 1989 Methods for evaluating fluid velocities in spectral simulations of turbulence. *J. Comput. Phys.* **83**, 96–125.

Batchelor, G. K. 1952 Diffusion in a field of homogeneous turbulence. II. The relative motion of particles. *Proc. Camb. Phil. Soc.* **48**, 345–362.

Batchelor, G. K. 1959 Small scale variation of convected quantities like temperature in a turbulent fluid. *J. Fluid Mech.* **5**, 113–133.

Batchelor, G. K., Howells, I. D. & Townsend, A. A. 1959 Small scale variation of convected quantities like temperature in a turbulent fluid. Part 2. The case of large conductivity. *J. Fluid Mech.* **5**, 134–139.

Batchelor, G. K. & Townsend, A. A. 1956 Turbulent diffusion. In *Surveys in Mechanics* (ed. G. K. Batchelor & R. M. Davies), pp. 352–399. Cambridge University Press.

Betchov, R. 1956 An inequality concerning the production of vorticity in isotropic turbulence. *J. Fluid Mech.* **1**, 497–504.

Blackburn, H. M., Mansour, N. N. & Cantwell, B. J. 1996 Topology of fine-scale motions in turbulent channel flow. *J. Fluid Mech.* **310**, 269–292.

Bogucki, D., Domaradzki, J. A. & Yeung, P. K. 1997 Direct numerical simulations of passive scalars with $Pr > 1$ advected by turbulent flow. *J. Fluid Mech.* **343**, 111–130

Borgas, M. S. & Sawford, B. L. 1996 Molecular diffusion and viscous effects on concentration statistics in grid turbulence. *J. Fluid Mech.* **324**, 25–54.

Brethouwer, G. 2000 Mixing of passive and reactive scalars in turbulent flows: a numerical study. PhD thesis, Delft University of Technology, The Netherlands.

Brethouwer, G. & Nieuwstadt, F. T. M. 1999 Mixing of weakly and strongly diffusive passive scalars in isotropic turbulence. In *Direct and Large-Eddy Simulation III, Proc. Isaac Newton Institute Symposium/ERCOFTAC Workshop* (ed. P. R. Voke, N. D. Sandham & L. Kleiser), pp. 311–322. Kluwer.

Buch, K. A. & Dahm, W. J. A. 1996 Experimental study of the fine-scale structure of conserved scalar mixing in turbulent shear flows. Part 1. $Sc \gg 1$. *J. Fluid Mech.* **317**, 21–71.

Buch, K. A. & Dahm, W. J. A. 1998 Experimental study of the fine-scale structure of conserved scalar mixing in turbulent shear flows. Part 2. $Sc \approx 1$. *J. Fluid Mech.* **364**, 1–29.

Canuto, C., Hussaini, M. Y., Quarteroni, A. & Zang, T. A. 1988 *Spectral Methods in Fluid Dynamics*. Springer.

Chong, M. S., Soria, J., Perry, A. E., Chacin, J., Cantwell, B. J. & Na, Y. 1998 Turbulence structures of wall-bounded shear flows using DNS data. *J. Fluid Mech.* **357**, 225–247.

Corrsin, S. 1953 Remarks on turbulent heat transfer: an account of some features of the phenomenon in fully turbulent regions. In *Proc. Iowa Thermodynamics Symposium*, pp. 5–30. State University of Iowa.

Debussche, A., Dubois, T. & Temam, R. 1995 The nonlinear Galerkin method. *Theoret. Comput. Fluid Dyn.* **7**, 279–315.

van Dop, H. 2001 The evaluation of a Lagrangian model for turbulent transport and chemistry. *Phys. Fluids* **13**, 1331–1342.

Dresselhaus, E. & Tabor, M. 1991 The kinematics of stretching and alignment of material elements in general flow fields. *J. Fluid Mech.* **236**, 415–444.

Durbin, P. A. 1980 A stochastic model of two-particle dispersion and concentration fluctuations in homogeneous turbulence. *J. Fluid Mech.* **100**, 279–302.

Eswaran, V. & Pope, S. B. 1988 An examination of forcing in direct numerical simulations of turbulence. *Comput. Fluids* **16**, 257–278.

Frisch, U. 1995 *Turbulence: the Legacy of A. N. Kolmogorov*. Cambridge University Press.

Fung, J. C. H., Hunt, J. C. R., Malik, N. A. & Perkins, R. J. 1992 Kinematic simulation of homogeneous turbulence by unsteady random Fourier modes. *J. Fluid Mech.* **236**, 281–318.

Fung, J. C. H. & Vassilicos, J. C. 1998 Two-particle dispersion in turbulentlike flows. *Phys. Rev.* E **57**, 1677–1690.

Gibson, C. H., Ashurst, W. T. & Kerstein, A. R. 1988 Mixing of strongly diffusive passive scalars like temperature by turbulence. *J. Fluid Mech.* **194**, 261–293.

Girimaji, S. S. & Pope, S. B. 1990 Material-element deformation in isotropic turbulence. *J. Fluid Mech.* **220**, 427–458.

Gonzalez, M. 2000 Study of the anisotropy of a passive scalar field at the level of dissipation. *Phys. Fluids* **12**, 2302–2310.

Holzer, M. & Siggia, E. D. 1994 Turbulent mixing of a passive scalar. *Phys. Fluids* **6**, 1820–1837.

Hunt, J. C. R., Kaimal, J. C. & Gaynor, J. E. 1988 Eddy structure in the convective boundary layer: new measurements and concepts. *Q. J. R. Met. Soc.* **114**, 821–858.

Jiménez, J., Wray, A. A., Saffmann, P. G. & Rogallo R. S. 1993 The structure of intense vorticity in isotropic turbulence. *J. Fluid Mech.* **255**, 65–90.

Jullien, M.-C., Paret, J. & Tabeling, P. 1999 Richardson pair dispersion in two-dimensional turbulence. *Phys. Rev. Lett.* **82**, 2872–2875.

Kerr, R. M. 1985 Higher-order derivative correlations and the alignment of small-scale structures in isotropic numerical turbulence. *J. Fluid Mech.* **153**, 31–58.

Kerstein, A. R. 2001 Kinematics of small scale anisotropy in turbulence. *Phys. Rev.* E **64**, 036306.

Kevlahan, N. K.-R. & Hunt, J. C. R. 1997 Nonlinear interactions in turbulence with strong irrotational straining. *J. Fluid Mech.* **337**, 333–364.

Komori, S., Hunt, J. C. R., Kanzaki, T. & Murakami, Y. 1991 The effects of turbulent mixing on the correlation between two species and on concentration fluctuations in non-premixed reacting flows. *J. Fluid Mech.* **228**, 629–659.

Kraichnan, R. H. 1974 Convection of a passive scalar by a quasi-uniform random straining field. *J. Fluid Mech.* **64**, 737–762.

Kurien, S., Aivalis, K. G. & Sreenivasan, K. R. 2001 Anisotropy of small-scale scalar turbulence. *J. Fluid Mech.* **448**, 279–288.

Métais, O. & Lesieur, M. 1992 Spectral large-eddy simulation of isotropic and stably stratified turbulence. *J. Fluid Mech.* **239**, 157–194.

Moisy, F., Willaime, H., Andersen, J. S. & Tabeling, P. 2001 Passive scalar intermittency in low temperature helium flows. *Phys. Rev. Lett.* **86**, 4827–4830.

Monin, A. S. & Yaglom, A. M. 1975 *Statistical Fluid Mechanics*, vol. II (ed. J. L. Lumley). MIT Press.

Mydlarski, L. & Warhaft, Z. 1998 Passive scalar statistics in high-Péclet-number grid turbulence. *J. Fluid Mech.* **358**, 135–175.

Nomura, K. K. & Elghobashi, S. E. 1992 Mixing characteristics of an inhomogeneous scalar in isotropic and sheared turbulence. *Phys. Fluids* A **4**, 606–625.

Ohkitani, K. 1998 Stretching of vorticity and passive vectors in isotropic turbulence. *J. Phys. Soc. Japan* **67**, 3668–3671.

Ooi, A., Martin, J., Soria, J. & Chong, M. S. 1999 A study of the evolution and characteristics of the invariants of the velocity-gradient tensor in isotropic turbulence. *J. Fluid Mech.* **381**, 141–174.

Orlandi, P. & Antonia, R. A. 2002 Dependence of the non-stationary form of Yaglom's equation on the Schmidt number. *J. Fluid Mech.* **451**, 99–108.

Overholt, M. R. & Pope, S. B. 1996 Direct numerical simulation of a passive scalar with imposed mean gradient in isotropic turbulence. *Phys. Fluids* **8**, 3128–3148.

Passot, T., Politano, H., Sulem, P. L., Angilella, J. R. & Meneguzzi, M. 1995 Instability of strained vortex layers and vortex tube formation in homogeneous turbulence. *J. Fluid Mech.* **282**, 313–338.

Pumir, A. 1994 A numerical study of the mixing of a passive scalar in three dimensions in the presence of a mean gradient. *Phys. Fluids* **6**, 2118–2132.

Richardson, L. F. 1926 Atmospheric diffusion shown on a distance-neighbour graph. *Proc. R. Soc. Lond.* A **110**, 709–737.

Ruetsch, G. R. & Maxey, M. R. 1991 Small-scale features of vorticity and passive scalar fields in homogeneous isotropic turbulence. *Phys. Fluids* A **3**, 1587–1597.

Ruetsch, G. R. & Maxey, M. R. 1992 The evolution of small-scale structures in homogeneous isotropic turbulence. *Phys. Fluids* A **4**, 2747–2760.

Sawford, B. L. 2001 Turbulent relative dispersion. *Annu. Rev. Fluid Mech.* **33**, 289–317.

Sawford, B. L. & Hunt, J. C. R. 1986 Effects of turbulence structure, molecular diffusion and source size on scalar fluctuations in homogeneous turbulence. *J. Fluid Mech.* **165**, 373–400.

Shraiman, B. I. & Siggia, E. D. 2000 Scalar turbulence. *Nature* **405**, 639–646.

Soria, J., Sondergaard, R., Cantwell, B. J., Chong, M. S. & Perry, A. E. 1994 A study of fine-scale motions of incompressible time-developing mixing layers. *Phys. Fluids* **6**, 871–884.

Sreenivasan, K. R. & Antonia, R. A. 1997 The phenomenology of small-scale turbulence. *Annu. Rev. Fluid Mech.* **29**, 435–472.

Squires, K. D. & Eaton, J. K. 1991 Measurements of particle dispersion obtained form direct numerical simulations of isotropic turbulence. *J. Fluid Mech.* **226**, 1–35.

Taylor, G. I. 1921 Diffusion by continuous movements. *Proc. Lond. Math. Soc.* **20**, 196–211.

Tennekes, H. & Lumley, J. L. 1972 *A First Course in Turbulence*. MIT Press.

Thomson, D. J. 1990 A stochastic model for the motion of particle pairs in isotropic high-Reynolds-number turbulence, and its application to the problem of concentration variance. *J. Fluid Mech.* **210**, 113–153.

Tong, C. & Warhaft, Z. 1994 On passive scalar derivative statistics in grid turbulence. *Phys. Fluids* **6**, 2165–2176.

Tsinober, A. 2000 Vortex stretching versus production of strain/dissipation. In *Vortex Dynamics and Turbulence Structure* (ed. J. C. R. Hunt & J. C. Vassilicos). Cambridge University Press.

Tsinober, A., Ortenberg, M. & Shtilman, L. 1999 On depression of nonlinearity in turbulence. *Phys. Fluids* **11**, 2291–2297.

Vedula, P., Yeung, P. K. & Fox, R. O. 2001 Dynamics of scalar dissipation in isotropic turbulence: a numerical and modelling study. *J. Fluid Mech.* **433**, 29–60.

Vincent, A. & Meneguzzi, M. 1994 The dynamics of vorticity tubes in homogeneous turbulence. *J. Fluid Mech.* **258**, 245–254.

Warhaft, Z. 2000 Passive scalars in turbulent flows. *Annu. Rev. Fluid Mech.* **32**, 203–240.

Yeung, P. K. 2001 Lagrangian characteristics of turbulence and scalar transport in direct numerical simulations. *J. Fluid Mech.* **427**, 241–274.

Yeung, P. K. & Pope, S. B. 1989 Lagrangian statistics from direct numerical simulations of isotropic turbulence. *J. Fluid Mech.* **207**, 531–586.

Zhou, T. & Antonia, R. A. 2000 Approximations for turbulent kinetic energy and temperature variance dissipation rates in grid turbulence. *Phys. Fluids* **12**, 335–344.